IAPv4 ocean temperature and ocean heat content gridded dataset

Lijing Cheng[1,11*], Yuying Pan[1,11], Zhetao Tan[1,11], Huayi Zheng[1,11], Yujing Zhu[1,11], Wangxu Wei[1,11], Juan Du[1], Huifeng Yuan[2,11], Guancheng Li[3], Hanlin Ye[1], Viktor Gouretski[1], Yuanlong Li[4,11], Kevin E. Trenberth[5,6], John Abraham[7], Yuchun Jin[4,11], Franco Reseghetti[8], Xiaopei Lin[9], Bing Zhang[4,11], Gengxin Chen[10, 11], Michael E. Mann[12], Jiang Zhu[1,11]

[1] Institute of Atmospheric Physics, Chinese Academy of Sciences, Beijing, China, 100029.

[2] Computer Network Information Center, Chinese Academy of Sciences, Beijing, 100083.

[3] Eco-Environmental Monitoring and Research Center, Pearl River Valley and South China Sea Ecology and Environment Administration, Ministry of Ecology and Environment, PRC, Guangzhou 510611, China.

[4] Institute of Oceanography, Chinese Academy of Sciences, Qingdao, China.

[5] National Center for Atmospheric Research, PO Box 3000, Boulder, CO 80307, USA.

[6] University of Auckland, Auckland, New Zealand.

[7] University of St. Thomas, School of Engineering, 2115 Summit Ave., St Paul, MN 55105, USA.

[8] Istituto Nazionale di Geofisica e Vulcanologia, 40127, Bologna, Italy.

[9] Frontier Science Center for Deep Ocean Multispheres and Earth System and Physical Oceanography Laboratory, Ocean University of China, Qingdao, China.

[10] State Key Laboratory of Tropical Oceanography, South China Sea Institute of Oceanology, Chinese Academy of Sciences, Guangzhou, China

[11] University of Chinese Academy of Sciences, Beijing, China.

[12] Dept. of Earth and Environmental Science, University of Pennsylvania, Philadelphia PA, USA

Correspondence to: Lijing Cheng (chenglij@mail.iap.ac.cn)

Abstract. Ocean observational gridded products are vital for climate monitoring, ocean and climate research, model evaluation, and supporting climate mitigation and adaptation measures. This paper describes the 4th version of the Institute of Atmospheric Physics (IAPv4) ocean temperature and ocean heat content (OHC) objective analysis product. It accounts for recent developments in quality control (QC) procedures, climatology, bias correction, vertical and horizontal interpolation, and mapping and is available for the upper 6000 m (119 levels) since 1940 (more reliable after ~1957) for monthly and $1° × 1°$ temporal and spatial resolutions. The IAPv4 is compared with the previous version, IAPv3, and to the other data products, sea surface temperatures (SSTs), and satellite observations. It has a slightly stronger long-term upper 2000 m OHC increase than IAPv3 for 1955-2023, mainly because of newly developed bias corrections. IAPv4 OHC 0-2000 m trend is also higher during 2005-2023 than IAPv3. The uppermost level of IAPv4 is consistent with independent SST datasets. The month-to-month OHC variability for IAPv4 is desirably less than IAPv3 and other OHC products investigated in this study, the trend of ocean warming rate (i.e., warming acceleration) is more consistent with the net energy imbalance at the top of the atmosphere than IAPv3, and the sea level budget can be closed within uncertainty. The gridded product is freely accessible at: http://dx.doi.org/10.12157/IOCAS.20240117.002 for temperature data (Cheng et al., 2024a) and http://dx.doi.org/10.12157/IOCAS.20240117.001 for ocean heat content data (Cheng et al., 2024b).

1. Introduction

Observational gridded products are essential for understanding the ocean, the atmosphere, and climate change; they support policy decisions and social-economy developments (Abraham et al., 2022; Abraham and Cheng, 2022; Cheng et al., 2022a). For instance, many of the climate indicators used in the Working Group I report of the 6th Intergovernmental Panel on Climate Change (IPCC-AR6-WG1) are based on gridded products (Gulev et al., 2021; IPCC, 2021), mainly because the raw oceanic data suffer from inhomogeneous data quality and irregular and incomplete data coverage (Abraham et al., 2013; Boyer et al., 2016; Cheng et al., 2022a; Meyssignac et al., 2019).

As more than 90% of the Earth's energy imbalance (EEI) in the past half-century has accumulated in the ocean, increasing ocean temperature (T) and ocean heat content (OHC) are essential climate variables for monitoring, understanding, and projecting climate change (e.g., Rhein et al., 2013; Hansen et al., 2011; Trenberth, 2022; Trenberth et al., 2009; von Schuckmann et al., 2020; Cheng et al., 2022). OHC also impacts air-sea and ice-sea interactions and thus exerts a considerable influence over the other components of the climate system. It provides critical feedback through energy, water, and carbon cycles (Cheng et al., 2022a; Trenberth, 2022; von Schuckmann et al., 2016). Substantial changes in ocean temperatures also profoundly impact ocean biogeochemical processes and ecosystems and are critical for ocean health and human society (Bindoff et al., 2019; Cheng et al., 2022a).

Many gridded T/OHC datasets have been produced by independent groups, and most of them are updated annually or more frequently (Cheng et al., 2022a; Good et al., 2013; Hosoda et al., 2008; Ishii et al., 2017; Levitus et al., 2012; Li et al., 2017; Meyssignac et al., 2019; Roemmich and Gilson, 2009). Most widely-used products are at $1° × 1°$ horizontal resolution and monthly temporal resolution from near-surface to at least 2000 m depth. Some products utilize all available *in situ* observations and span at least half a century, prominent examples being the data products compiled by the Institute of Atmospheric Physics (IAP) (Cheng and Zhu, 2016; Cheng et al., 2017) from 1940-present; Japan Meteorological Agency (JMA) (Ishii et al., 2017) from 1955-present; National Centers for Environmental Information (NCEI), National Oceanic and Atmospheric Administration (NOAA) from 1950-present (Levitus et al., 2012); and University of California since 1949 (Bagnell and DeVries, 2021). As Argo data has achieved near-global upper 2000 m open ocean coverage since ~2005, many Argo-based or Argo-only gridded products are available. Examples include gridded products from SCRIPPS after 2004 (Roemmich and Gilson, 2009); China Argo Real-time Data Center since 2005 (Li et al., 2017); and Copernicus since 2005 (von Schuckmann and Le Traon, 2011). These products usually span from ~2005 to the present for the upper ~2000 m. These data benefit from the high quality of Argo data but are not fully resolving polar regions, shallow waters, and regions with complex topography.

In 2016, the IAP group provided its first gridded product for the upper 700 m ocean (Cheng and Zhu, 2016) by merging all available observations since 1960. With a revised mapping method and a thorough evaluation process with synthetic observations, an update

92 (IAP version 3, IAPv3) became available in 2017 for the upper 2000 m ocean with data

93 since the 1950s (Cheng et al., 2017). The IAPv3 has supported scientific research, climate

94 assessment reports, and monitoring practices (Bindoff et al., 2019; Gulev et al., 2021;

95 WMO, 2022).

96   After the release of IAPv3, there has been progress with observation data quality

97 control and new/updated techniques for temperature data processing and reconstruction.

98 For example, Gouretski et al. (2022) found that old Nansen cast bottle data contained

99 systematic biases that impacted the T/OHC data before 1990. Revisions are also available

100 to the bias corrections for the Mechanical Bathythermographs (MBT) and eXpendable

101 Bathythermographs (XBT) data (Cheng et al., 2014; Gouretski and Cheng, 2020), mainly

102 impacting the data within 1940–2005. Tan et al. (2023) developed a new quality-control

103 system that advances the detection of outliers after accounting for the non-Gaussian

104 distribution of local temperatures in determining the local climatological range. The impact

105 of inhomogeneous vertical resolution of temperature profiles has been recognized

106 previously (Cheng and Zhu, 2014) and received more attention recently (Li et al., 2020)

107 with a new vertical interpolation approach (Barker and McDougall, 2020). Upgrading the

108 product with new developments is important to better support the ocean/climate research

109 and climate assessments.

110   This manuscript discusses the revisions to the IAP ocean objective analysis product

111 (IAPv4) since the publication of the IAPv3 (Cheng et al., 2017). The data and methods are

112 introduced in Section 2 and the results are presented in Section 3, with analyses of the

113 character of the IAPv4 on regional and global scales and at various time scales. The EEI

114 and sea level budgets based on the new data product are also investigated. A summary and

115 discussion are provided in Section 4, with some remaining issues and outlooks being

116 discussed.

117

118 **2. Data and Methods**

119 **2.1 Data source**

120   The majority of the *in situ* measurements used to create the data product come from

121 the World Ocean Database (WOD), downloaded in September 2023. Data from all

122 instrument types are used, including XBTs (Goni et al., 2019), Argo (Argo 2000),

123 Conductivity/Temperature/Depth profilers (CTDs), MBTs, bottles, moorings, gliders,

124 Animal Borne Ocean Sensors (McMahon et al., 2021) and others (Boyer et al., 2018) (Fig.

1). There is a total of 17,634,865 temperature profiles from January 1940 to September 2023 (Fig. 1a). MBT, XBT, Nansen Bottle and CTD data are the major instruments before 2000 (Fig. 1a, b). The spatial coverage of these data increased to >30% in 1960 and >70% in the late 1960s for $1° × 1° × 1$-year resolution. After 2005, there is a huge number of GLD and APB data, and as they are mainly distributed in the polar regions (APB) and coastal regions (GLD) (Fig. 1a), their spatial coverage is usually less than 5% for $1° × 1° × 1$ year resolution. By contrast, the Argo data cover most of the global open ocean since ~2005 (Fig. 1b).

Argo data are processed following the recommendations of the Argo community. Adjusted data are used where applicable. Both Delayed- and Real-Time Argo data have been incorporated in IAPv4. As Real-Time Argo data have only passed automated, simple QC tests in real-time, these data may still contain temperature, pressure, and salinity values affected by unknown errors. However, through a sensitivity study, Cheng (2024) indicated that including Real-Time Argo data does not bias the OHC calculation for the IAP analysis. Nevertheless, IAP data are updated frequently (every 1-3 months): each time the updated Argo data is used, the T/OHC fields are recalculated following the recommendation by the Argo group (Wong et al., 2020). The data from the Argo floats in the "grey list" have been removed from the calculation (https://data-argo.ifremer.fr/).

To complement the WOD with relatively less data in the Arctic and coastal regions of the Northwest Pacific, this presented product also uses data from other sources. The majority of these data are from the Chinese Academy of Sciences Ocean Science Data Center (Zhang et al., 2024), and some data are rescued from the old documents of marine surveys. All these data will be publicly available. There are a total of 85,990 additional temperature profiles, about 0.50% of the data, which is expected to improve the reconstruction in these data-sparse regions (compared with IAPv3 and other products).

The *in situ* data have been processed as described in a flow chart in Figure 2. In the following sections, the key techniques of data processing are introduced.

153
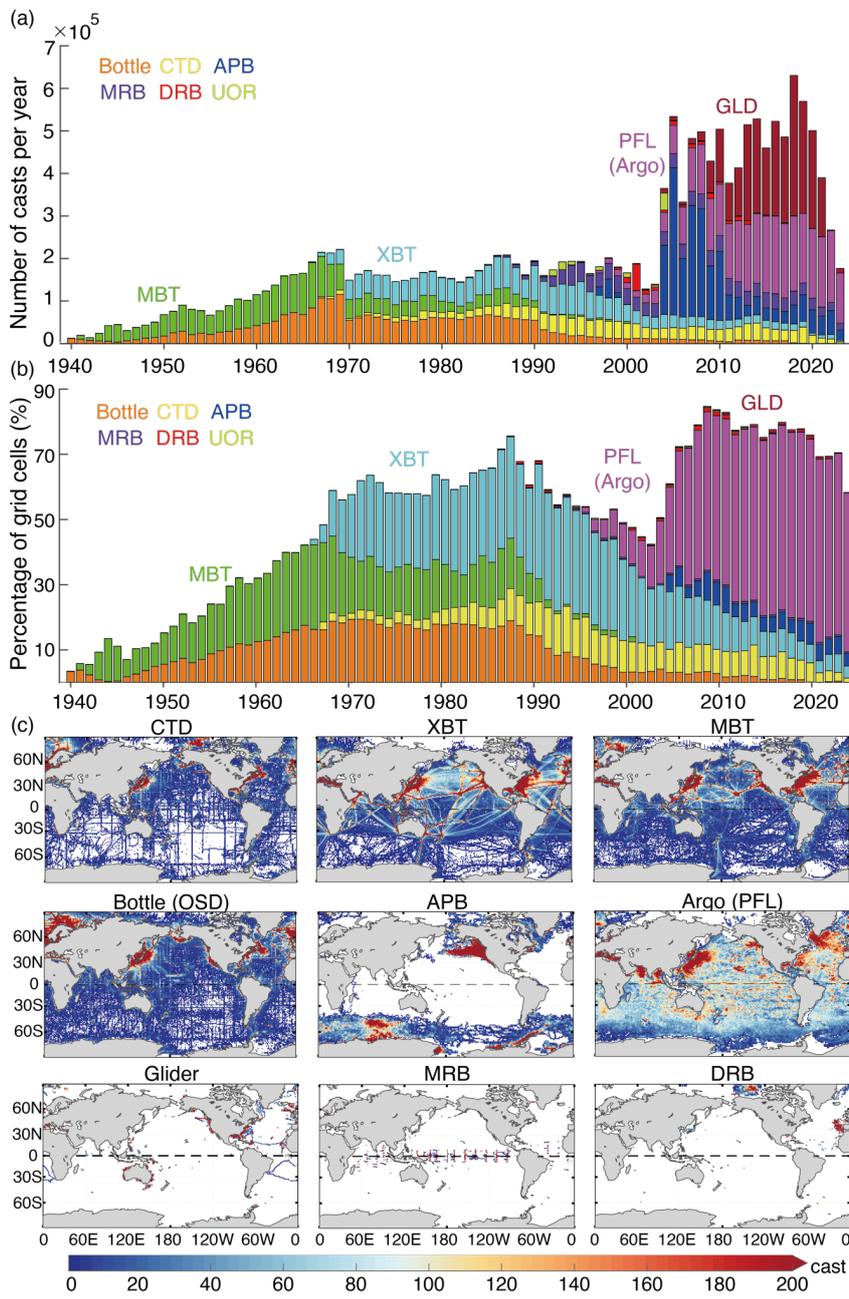
Figure 1: (a) Yearly number of temperature casts for different instruments; (b) percentage coverage (%) of ocean data for each instrument, calculated as the ratio between the number of 1° × 1° × 1 year grid cells observed by each instrument and the total number of ocean grids; (c) number of subsurface temperature casts in 1-degree grid boxes from 1940 to 2023 collected by different instruments: CTD (Conductivity/Temperature/Depth), XBT (eXpendable BathyThermographs), MBT (Mechanical BathyThermograph), Bottle, APB (Animal mounted Pinniped Borne), PFL (Profiling Floats, i.e. Argo), GLD (Glider), MRB (Moored Buoy), and DRB (Drifting Buoy).
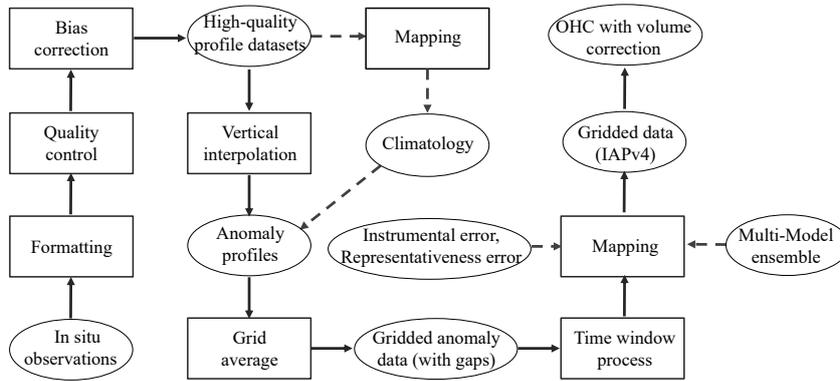
Figure 2: Flow chart of the IAP data reconstruction processes from the raw *in situ* observations to gridded data (IAPv4) and OHC estimates. The ellipses indicate the data (including data for error estimates), and the rectangle boxes show the techniques used to process the data.

2.2 Data quality control

The quality control (QC) procedure aims to identify spurious measurements (including outliers) and data with incorrect metadata through a set of quality checks and ensures the quality of the *in situ* dataset (Tan et al., 2022). There is growing evidence that QC is critical for accurate temperature/OHC reconstruction, as shown by Tan et al., (2023) where two different QC systems produced a difference of approximately 15 % (~7 %) in the OHC 0-2000 m trend from 1955 to 1990 (2005-2021). Unfortunately, the impact of QC on OHC

177 estimates has not been evaluated in previous community-assessments on T/OHC

178 uncertainty (Boyer et al., 2016; Lyman et al., 2010). In this study, the QC procedure

179 follows the CAS-Ocean Data Center (CODC) Quality Control system, named CODC-QC

180 (Tan et al., 2023), where only the "good" data (flag=0) are used.

181 The CODC-QC system (Tan et al., 2023) has the following strengths, which make it

182 particularly suitable for T/OHC reconstruction:

183 1) A new local climatological range is defined in this CODC-QC system to identify

184 the outliers. Unlike many existing QC procedures, no assumption is made of a Gaussian

185 distribution law in the new approach, as the oceanic variables (e.g., temperature and

186 salinity) are typically skewed. Instead, the 0.5 % and 99.5 % quantiles are used as

187 thresholds in CODC-QC to define the local climatological parameter ranges.

188 2) Local climatological ranges change with time to account for the long-term trends of

189 ocean temperature accompanied by more frequent extreme events (e.g., Oliver et al., 2018;

190 Sun et al., 2023). Previously, the use of the static local ranges tended to remove too many

191 "extreme values" (at the tails of the temperature distributions) associated with climate

192 change in recent years that were actually real, leading to a QC-procedure related bias in the

193 gridded dataset and OHC estimate (Tan et al., 2023).

194 3) In addition, local climatological ranges for the vertical temperature gradient are

195 constructed to account for the variability of 'vertical shape', increasing the ability of the

196 scheme to identify spurious profiles.

197 4) The QC procedure is instrument-specific, accounting for characteristics inherent to

198 particular instrumentation types. For example, XBT digital recording systems are allowed

199 to continue to record beyond the rated terminal depth suggested by manufacturers (T7/DB

200 probes below 760 m; T4/T6 below 460 m; T5 below 1830 m). Below the rated maximum

201 depth, the XBT wire often breaks, leading to a characteristic change in recorded

202 temperature values. The new QC procedure effectively identifies such profiles.

203 5) The thorough evaluation of the QC procedure performance and the application of

204 the QC procedure to the manually QC-ed datasets (Thresher et al., 2008; Gouretski and

205 Koltermann, 2004) demonstrated the effectiveness of the proposed scheme in removing

206 spurious data and minimizing the percentage of mistakenly flagged good data.

207 Being applied to the entire temperature profile dataset the CODC-QC procedure

208 identifies 6.22 % of all temperature measurements as outliers. The rejection rates

209 (definition follows Tan et al., 2023) vary among instrumentation types (3.73 % for CTD,

210   1.97 % for Argo, 12.06 % for XBT, 4.93 % for MBT, 6.54 % for bottle, 5.92 % for APB,

211   4.54 % for DRB, 2.55 % for MRB). The overall percentage of outliers decreases over time

212   from ~5 % in the 1940s to ~2.5 % in the 2020s, reflecting the progressive improvement of

213   the instrumentation (Fig. 3). A rejection rate maximum (~12 %) during 2000~2010 is

214   linked to the XBT data, which are especially abundant in the 800–1100m layer and are

215   characterized by higher rejection rate below the maximum depth (Tan et al., 2023). The

216   generally higher rejection rate below 4000 meters is related to the gross errors (such as

217   measurements cooler than -2°C, big spikes, etc.) and the occurrence of the constant values

218   (recorded values don't change with depth). For example, the higher rejection rate within

219   2008-2009 below 4000 meters is because of the gross errors in the CTD data.
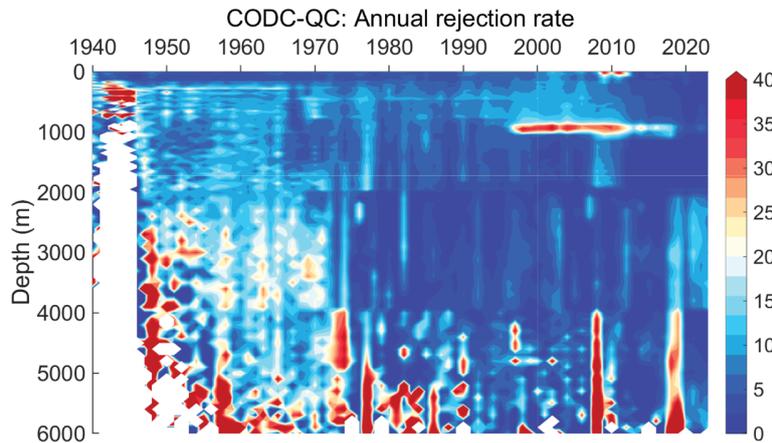
220

221   **Figure 3: The rejection rate (%) after CODC-QC as a function of calendar year and**

222   **depth.**

223

224   **2.3 Bias correction**

225   It is well known that data from several instrument types can exhibit biases both in

226   temperature and depth. Temperature profiles obtained using XBTs and MBTs provide an

227   example of biased data, especially because of uncertainties in the depth of measurement.

228   Gouretski and Koltermann (2007) demonstrated their significant impact on the magnitude

229   and variability of the global OHC estimates. That study triggered a series of publications

230   where different bias correction schemes have been suggested for XBT (Gouretski and

231 Reseghetti, 2010; Abraham et al., 2013; Cheng et al., 2016; Levitus et al., 2009; Wijffels et

232 al., 2008), MBT (Gouretski and Cheng 2020; Levitus et al., 2009) and other instruments

233 (Fig. 2). In the compilation of IAPv4, newly developed bias correction schemes are

234 applied.

235   The XBT temperature bias was found to be generally positive, as large as ~0.1 °C

236 before 1980 on the global 0–700 m average, diminishing to less than 0.05 °C after 1990

237 (Gouretski and Koltermann 2007; Wijffels et al., 2008). Here, we use an updated XBT bias

238 correction scheme (Cheng et al., 2014) to correct both depth and temperature biases in

239 XBT data, following the community recommendation (Cheng et al., 2016; Goni et al.,

240 2019). The depth and temperature biases depend on ocean temperature, probe type, and

241 time. An inter-comparison among several correction schemes rated the CH14 scheme the

242 most successful (Cheng et al., 2018). Using XBT and collocated CTD data, we updated the

243 CH14 scheme by re-calculating bias corrections between 1966-2016 and extending them

244 for the years 2017 to 2023.

245   Comparison with collocated reference CTD profiles recently revealed significant

246 biases in the old hydrographic profiles obtained by means of Nansen bottle casts

247 (Gouretski et al., 2022). Both depth and temperature measurements of bottle casts were

248 found to be biased, and the proposed correction scheme was also implemented in IAPv4.

249 The thermal bias is related to the time needed to bring the mercury thermometers in

250 equilibrium with the ambient temperature after the completion of the hydrographic cast.

251 The depth bias indicates an overestimation of the bottle depth due to the wire's deviation

252 from the vertical position and is mostly related to the hydrographic casts where the

253 thermometrical method of sample depth determination was not used. The correction

254 scheme includes a constant thermal bias of -0.02 °C and a depth- and time-variable depth

255 bias.

256   The MBT bias is as large as 0.28 °C before 1980 for the global average and reduces to

257 less than 0.18 °C after 1980 for the 0~200 m average. IAPv3 used Ishii and Kimoto, (2009)

258 (IK09) scheme to correct MBT bias, while a new scheme proposed by Gouretski and

259 Cheng, (2020) (GC20) is adopted in IAPv4. This shift is made because our assessment

260 indicates the under-correction of MBT bias by the IK09 scheme within the upper 120 m

261 and over-correction in the deeper layer, whereas GC20 corrects both depth and temperature

262 biases. GC20 also found the MBT bias to be country-dependent, explained in terms of

263 different instrumentation characteristics and working procedures. Therefore, the time-

264   varying bias corrections are applied separately for the MBT profiles obtained by ships

265   from the United States, Soviet Union/Russia, Japan, Canada, and Great Britain. Data from

266   all other countries are corrected using a globally averaged correction.

267   Finally, thermal biases were recently reported for the data obtained by different kinds

268   of data loggers attached to marine mammals (APB). Gouretski et al. (2024) analysed

269   temperature profiles obtained between 2004 and 2019 in the high and moderate latitudes of

270   both hemispheres. Comparison with the collocated reference CTD and Argo float data

271   revealed a systematic negative thermal offset (average value -0.027 °C) for mammal

272   temperature profiles from SRDL (satellite-related data loggers). For the less accurate data

273   from TDR (Temperature-Depth-Recorders), the comparison revealed a small positive

274   temperature bias of 0.02 °C and the depth (pressure) bias indicating depth overestimation.

275

276   **2.4 Climatology**

277   For IAP and other data product generators, horizontal interpolation (mapping) is

278   applied on a temperature anomaly field after removing a monthly climatology; thus, a pre-

279   defined climatology field with an annual cycle is mandatory (Fig. 2). The accuracy of the

280   climatology field is one of the key sources of uncertainty in reconstruction because the

281   error in climatology will propagate into the anomaly field, impact the spatial dynamical

282   consistency, and the accuracy of the reconstruction (Cheng and Zhu, 2015; Lyman and

283   Johnson, 2014; Boyer et al., 2016).

284   In IAPv4, the adjusted mapping procedure (see below) has been applied to reconstruct

285   the climatology field (Table 1). The merit of using IAP mapping for climatology is its

286   ability to better represent the spatial anisotropy of temperature variability (non-Gaussian

287   distribution). Unlike IAPv3, where the 1990–2005 reference period was used, IAPv4 uses

288   data between 2006 and 2020 to construct 12 monthly climatologies, taking advantage of

289   more reliable data combined with better and more homogeneous spatial and temporal

290   coverage in the last two decades (Table 1). Following the recommendation in Cheng and

291   Zhu, (2015), a relatively short period of 15-year is used because climatology constructed

292   with longer period of data will result in different baselines at different locations (i.e., the

293   baseline shifted to earlier years in the middle latitudes of the North Hemisphere and the

294   baseline shifted to more recent years in the Southern Hemisphere) and this inconsistency

295   will violate the spatial structure of the anomaly field (Cheng and Zhu, 2015). Recent

developments from other groups, such as Li et al., (2022), include the choice of a short-period climatology.

IAPv4 used an 800 km influencing radii in climatology reconstruction, smaller than the 20° for IAPv3, to more properly account for the rapid change of temperatures with distance. There is a trade-off between data availability and the size of the influence radius. Using radii smaller than 500 km does not ensure a global fractional coverage (defined as the fraction of the total ocean area obtained by the mapping method) because of data sparseness (Cheng, 2024). As our tests suggest, using 500~800 km results in very similar reconstructions of climatology, therefore, 800 km is adopted.

2.5 Vertical interpolation

The vertical resolution of ocean temperature profiles changed dramatically over time associated with instrument evolution and the increase of data storage capability. For instance, the global mean vertical resolution at 500 m level changed from ~100 m in the 1960s to less than 10 m during the 2010s (Li et al., 2020). Vertical interpolation of the raw profiles on standard levels is a critical process (Fig. 2): Cheng and Zhu (2014) indicated that the use of linear or spline vertical interpolation methods can bias the temperature reconstruction and OHC estimation (Barker and McDougall, 2020; Li et al., 2020; Li et al., 2022). IAPv3 used the (Reiniger and Ross, 1968) (RR) method. Recently, Barker and McDougall (2020) proposed a new approach using multiple Piecewise Cubic Hermite Interpolating Polynomials (PCHIPs) to minimize the formation of unrealistic water masses by the interpolation procedure.

Because the largest difference between interpolation methods is found mostly for the low-resolution profiles (e.g., old Nansen casts), in practice, extremely low vertical resolution profiles had to be removed to reduce the uncertainty in interpolation. In IAPv4, this procedure is optimized compared to IAPv3, and only parts of profiles with a sufficient vertical resolution are used. The thresholds for the vertical resolution are set by 50 m in the upper 200m, 200m between 200 m and 1000 m, 500 m between 1000 m and 2000 m, and 600m between 2000 m and 6000 m. As no interpolation method can adequately interpolate temperature for the vertical resolution beyond these thresholds, interpolation is not performed in such cases to avoid errors (these extreme low-resolution data are not used in further processing). Under this limitation for IAPv4, we still apply the RR method for temperature profiles.

329   Finally, IAPv4 extends the set of standard vertical levels with a total of 119 levels
330 from 1 m to 6500 m (79 levels within the upper 2000 m) compared to 41 levels in IAPv3
331 between 1 m and 2000 m (Table 1). The increase in vertical resolution is critical for
332 accurately representing the mixed layer, as investigated below.
333
334 **2.6 Grid average and mapping**
335   The anomaly profiles are obtained by subtracting the monthly mean climatology from
336 the vertically interpolated profiles. These anomalies are then averaged (arithmetic mean)
337 into a $1° \times 1°$ grid at each standard level ($1° \times 1°$ gridded average field) (Fig. 2). Due to the
338 general data sparsity, variable time windows (larger than one month) are used for monthly
339 reconstructions to ensure a truly global analysis (Supplementary Table 1). This process
340 takes advantage of the larger persistence of anomalies (generally smaller monthly and
341 inter-annual variability) in the deep ocean than in the upper ocean and thus is physically
342 grounded. Specifically, after 2005, data within a three-month window are merged to
343 provide a monthly reconstruction for each layer of the upper 1950 m. Before 2005, a time-
344 varying and depth-varying time window is used, and it is generally smaller in the upper
345 ocean and wider in the deeper ocean (Supplementary Table 1). Below 2000 m, a 5-year
346 (60-month) window is adopted. The use of a time window will reduce the monthly
347 variance compared to other datasets, which is likely too high compared with independent
348 Earth's Energy Imbalance data at the top of the atmosphere (Trenberth et al., 2016).
349   Mapping interpolates the gridded (e.g., box-averaged) observations horizontally into a
350 spatially complete map (Fig. 2) because not all $1° \times 1°$ boxes are filled with data. (Fig. 2).
351 IAPv4 adopted a similar mapping approach (Ensemble Optimal Interpolation with dynamic
352 ensemble: EnOI-DE) as in IAPv3 introduced in Cheng and Zhu (2016) and Cheng et al.,
353 (2017) but with the following modifications:
354   1) the largest influence radius has changed from 20° in the upper 700 m (25° at 700–
355 2000 m) in IAPv3 to 2,000 km in the upper 700 m (2,500 km at 700–6000 m) in IAPv4, to
356 account for the reduced distance between two longitudes from tropics to the polar regions.
357 This change mainly helps to improve the reconstruction in the high-latitude regions;
358   2) The three iterative runs are taken to effectively bring in different scales of
359 variability with influencing radius changing from 2,000 km (2,500 km at 700–6000 m) to
360 800 km and 300 km, respectively, based on the tests presented in Cheng and Zhu (2016)
361 and Cheng et al., (2017);

3) For each month, IAPv3 used 40 model simulations (historical runs) from the Coupled Model Intercomparison Project phase 5 (CMIP5) to provide a flow-dependent ensemble, which is then constrained by observations to provide optimized spatial covariance. IAP mapping uses model-based covariance because we argue that spatial covariance can never be satisfactorily parametrized by some simple basic functions (such as Gaussian) given its complexity. With model-based, flow-dependent, and dynamically-consistent covariance, the IAP mapping provides a more realistic reconstruction than other approaches based on Gaussian-based parameterized covariance, as evaluated by many studies (Cheng et al., 2017; Cheng et al., 2020; Dangendorf et al., 2021; Nerem et al., 2018).

4) The observation error variance (**R**), which represents the error of the observations, is updated in IAPv4 as follows. **R** consists of both the instrumental error (**Re**) due to inaccuracy and the representativeness error (**Rr**) due to the need to represent the spatial (at 1° by 1° and 1 m standard grid depths) and temporal (1 month) averages from a limited numbered of observations (Cheng and Zhu, 2016):

$$\mathbf{R} = \mathbf{Re} + \mathbf{Rr} = (\sum_1^M \boldsymbol{Ei})/M + \sigma^2/M,$$

where M observations exist for a given grid cell. $\boldsymbol{Ei}$ is the instrument's precision for each individual observation, assuming random error (the basic assumption is that after bias correction, the systematic errors can be eliminated). **Re** in each grid cell is set to the mean of the typical precision of the different instruments contributing data in the cell, which is set according to IQuOD (International Quality-Controlled Ocean Database) specification (Cowley et al., 2021). σ^2 represents the variance of the various temperature measurements against the monthly mean value. The data from 2005 to 2022 are used to calculate σ^2 in each grid because of greater data abundance and quality compared to earlier times.

As the representativeness error (**Rr**) is expected to be flow-dependent (i.e., the error is expected to be higher in areas with a large gradient of the flow speed and regions of higher variability), more observations are required to represent the mean value. Figure 4 shows a larger variance (σ^2) in the boundary-current regions and near the Antarctic Circumpolar Current (ACC) in the upper ocean (e.g., 10 m, 200 m, 500 m). At 200 m, it shows a larger σ^2 in the Western Pacific Ocean, corresponding to the large thermocline variations at this layer. Below 1000 m, larger σ^2 along the ACC frontal regions and in the North Atlantic Ocean occur because of a stronger mixing and convection in these regions.

394   The uncertainty in the derived gridded reconstruction is also based on the EnOI

395   framework formulated by Cheng and Zhu, (2016). The uncertainty accounts for

396   instrumental, sampling and mapping errors. Other error sources, including the choice of

397   climatology, vertical interpolation, bias corrections, and QC, are not considered in this

398   uncertainty estimate. Therefore, a more thorough uncertainty quantification method is

399   needed, and this is under development in a separate study.
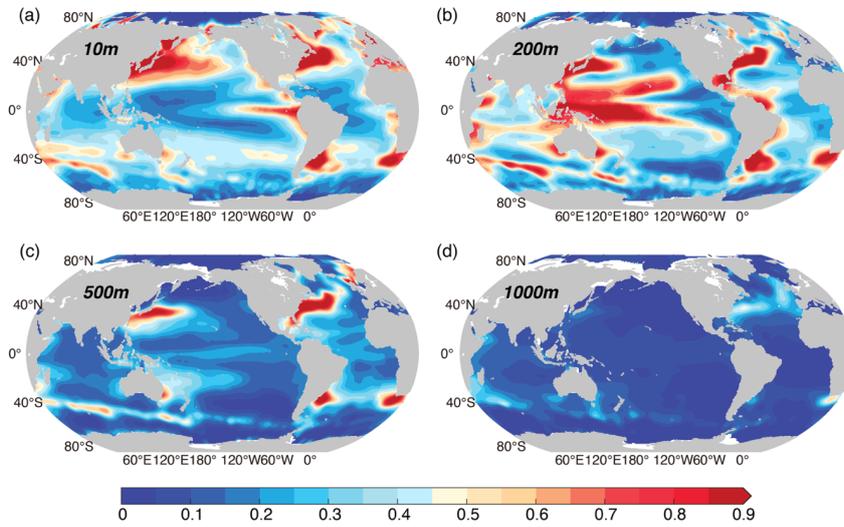
400

401   **Figure 4: Variance (σ^2) of ocean temperature at several representative layers.** (a)

402   10 m, (b) 200 m, (c) 500 m and (d) 1000 m. The unit is °C^2.

403

404   **Table 1.** General information on IAPv4 and IAPv3 data products.

	IAPv3	**IAPv4**
Horizonal resolution	Global (1° × 1°)	Global (1° × 1°)
Vertical levels	41 levels from 1 m to 2000 m (1, 5, 10, 20, 30, 40, 50, 60, 70, 80, 90, 100, 120, 140, 160, 180, 200, 250, 300, 350, 400, 450, 500, 550, 600, 650, 700, 750, 800, 850, 900, 1000, 1100, 1200, 1300, 1400, 1500, 1600, 1700, 1800, 2000)	119 levels from 1 m to 6000 m (1, 5, 10, 15, 20, 25, 30, 35, 40, 45, 50, 55, 60, 65, 70, 75, 80, 85, 90, 95, 100, 110, 120, 130, 140, 150, 160, 170, 180, 190, 200, 220, 240, 260, 280, 300, 320, 340, 360, 380, 400, 425, 450, 475, 500, 525, 550, 575, 600, 625, 650, 675, 700, 750, 800, 850, 900, 950, 1000, 1050, 1100, 1150, 1200,

		1250, 1300, 1350, 1400, 1450, 1500, 1550, 1600, 1650, 1700, 1750, 1800, 1850, 1900, 1950, 2000, 2100, 2200, 2300, 2400, 2500, 2600, 2700, 2800, 2900, 3000, 3100, 3200, 3300, 3400, 3500, 3600, 3700, 3800, 3900, 4000, 4100, 4200, 4300, 4400, 4500, 4600, 4700, 4800, 4900, 5000, 5100, 5200, 5300, 5400, 5500, 5600, 5700, 5800, 5900, 6000)
Time period and resolution	1940–2022 (reliable data after 1955), monthly	1940–present (reliable data after 1955), monthly
Quality-control	WOD (Garcia et al., 2018)	CODC-QC (Tan et al., 2023)
Vertical interpolation	RR (Reiniger and Ross, 1968) interpolation	RR (Reiniger and Ross, 1968) interpolation
Climatology	IAP climatology: simple gridded average and then spatial interpolation with distance-weighted average	Improved IAP reconstruction with EnOI approach
XBT bias correction	CH14 (updated in 2018)	CH14 (revised and updated in 2023)
MBT bias correction	IK09 (Ishii and Kimoto, 2009)	GC20 (Gouretski and Cheng, 2020)
APB bias correction	None	GCR24 (Gouretski et al., 2024)
Bottle bias correction	None	GCT22 (Gouretski et al., 2022)
Mapping	EnOI-DE with influencing radius of 20, 8, 3 degrees, iteratively.	EnOI-DE with influencing radius of 2000, 800, 300 km, iteratively. Representative error updated with 2005-2022 observations. The radius of influence does not cross the land.
Uncertainty	Given by EnOI framework accounting for instrumental error and horizonal sampling/mapping error	Given by EnOI framework accounting for instrumental error and horizonal sampling/mapping error
DOI	/	http://dx.doi.org/10.12157/IOCAS.20240117.002 for temperature data (Cheng et al., 2024a) and http://dx.doi.org/10.12157/IOCAS.20240117.001 for ocean heat content data (Cheng et al., 2024b)

405

2.7 OHC calculation and volume correction

Based on the gridded temperature reconstruction (Table 1), OHC in each grid is calculated as OHC $(x, y, z) = c_p \iiint_{V(x,y,z)} \rho T dV(x,y,z)$. following TEOS-10 standards, where c_p is a constant of $\sim$ 3991.9 J (kg K)$^{-1}$ according to the new TEOS-10 standard formulation as conservative temperature and absolute salinity are used, ρ is potential density in kg m^{-3}, and T is conservative temperature measured in degrees Celsius (here it is anomaly relative to the 2006–2020 baseline) (Cheng et al., 2022a).

As OHC is an integrated metric over a specific ocean volume, properly identifying ocean volume is critical, especially in shallow waters. Previous studies found a 10–20 % difference in the OHC trend in recent decades between different land-ocean masks (von Schuckmann and Le Traon, 2011; Meyssignac et al., 2019; Savita et al., 2022). Specifically, in marginal sea areas with complex topography, $1° \times 1° \times \Delta z$ grid boxes (where Δz is the depth range of the grid box) near coasts and islands typically cover both ocean and land areas but are assigned to represent land or ocean only. Thus, the gridded ocean temperature datasets are subjected to errors from inaccurate land-sea attribution. Here, we offer a volume correction (VC) for these grid boxes to improve the OHC estimate, as follows.

For each $1° \times 1° \times \Delta z$ grid box, we introduce a VC factor (denoted as F_{VC}) to correct the OHC values: OHC$_{VC}$ (x, y, z) = OHC (x, y, z) × F_{VC} (x, y, z). First, we assume the seawater volume distribution in 1 arc-minute topographic data of ETOPO1 as "truth". No correction is needed if a box is assigned to ocean according to ETOPO1 data, thus, F_{VC}=1. If a fraction of a $1° \times 1° \times \Delta z$ grid box is land according to ETOPO1 and IAP data includes T/OHC values, the F_{VC} is represented by the fraction of the ocean volume in this box (illustrated in Fig. 5), and the volume for OHC calculations can be corrected with F_{VC}(i). In a grid box, if there is no IAP data (i.e., it is land according to the IAP mask), but this box contains some ocean volume according to ETOPO1 data, we define F_{VC} (a) again as the fraction of the ocean volume in this box, and then this F_{VC}(a) is added to the adjacent grid boxes where there are values in IAP data. If all the adjacent grid boxes contain no data, the volume is equally redistributed to the diagonal boxes (Fig. 5). The volume is discarded if there is no data in all adjacent and diagonal boxes.

436   With this approach, the VC factor in each grid box is a sum of two components: a

437 local adjustment $F_{VC}(i)$ and a redistribution from the adjacent grids:

438   $F_{VC}(a))$: $F_{VC} = F_{VC}(i) + F_{VC}(a)$,

439   To avoid misidentification of sea ice, we performed VC only on the global grid points

440 within 60 °S to 60 °N. Eventually, we obtained a three-dimensional FVC that fits the IAP

441 grids (119 × 360 ×180; depth coverage to 6000 m) and used it to compute OHC. The VC

442 applied to ~15% of all the $1° × 1° × \Delta z$ grid boxes of IAPv4 ocean grid boxes (with $F_{VC} \neq$

443 1) for the entire 0-6000 m ocean and ~10% grid boxes of the upper 2000 m. Since the open

444 ocean accounts for the vast majority of the global ocean volume, the influence of the VC

445 method on the global OHC trend is small. For example, the upper 2000 m OHC trend with

446 VC is ~0.15% (~0.45%) smaller than without VC from 1958-2023 (2005-2023) for IAPv4.

447 However, it can significantly affect regional OHC estimates, especially in regions with

448 complex topography. For example, the Maritime Continent region's 0-2000 m OHC trend

449 is reduced by 6.9% (4.2%) after applying VC from 1958-2023 (2005-2023) (Jin et al.,

450 2024).
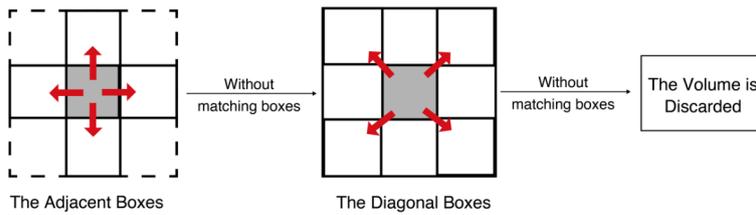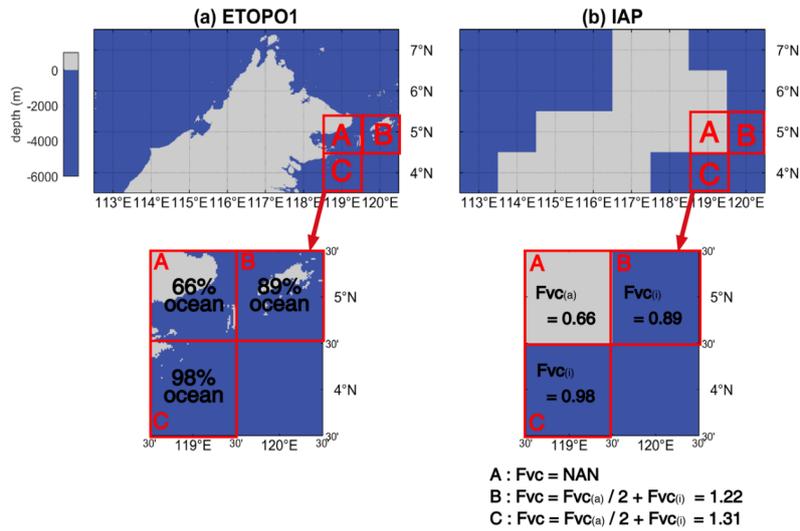
Figure 5: An example explaining the Volume Correction algorithm. (a) Bathymetry derived from ETOPO1. (b) Bathymetry in IAPv4 analysis.

2.8 Independent datasets for comparison and evaluation

Four Sea Surface Temperature (SST) datasets are used to evaluate the upper-most layer (1 m) of IAPv4, including Extended Reconstructed SST version 5 (ERSST5) (Huang et al., 2017); Japan Meteorological Agency Centennial Observation-Based Estimates of SSTs version 1 (COBE1) (Ishii et al., 2005), and its version 2: COBE2 (Hirahara et al., 2014); Hadley Centre Sea Ice and Sea Surface Temperature dataset (HadISST) (Rayner et al., 2003). The anomalies relative to a 2006-2020 average were computed by removing the monthly climatology. Measurements of SST are made *in situ* by means of thermometers or retrieved remotely from infrared and passive microwave radiometers on satellites (Kennedy, 2014; O'Carroll et al., 2019). Satellite SST observations began in the early

465 1980s. *In situ* SST observations go back to the 19th century and involve many different
466 measurement methods, including wooden and later insulated metal buckets to collect water
467 samples, engine room inlet measurements, and sensors on moored and drifting buoys
468 (Kennedy, 2014). The subsurface temperatures are collected as "profiles" which contain
469 multiple measurements at discrete vertical levels. Because of the differences in observation
470 systems, SSTs are fundamentally different in their temporal and spatial coverage and
471 temporal extent compared to subsurface observations on which OHC estimates rely. SST
472 measurements also have different uncertainty sources and error structures; thus, the two
473 systems are typically treated as independent data sources and have been used for cross-
474 validation (Gouretski et al., 2012).

475   An independent in situ observation dataset in the Labrador Sea is used to evaluate
476 IAPv4. This dataset, provided by the Bedford Institute of Oceanography (BIO)
477 (Yashayaev, 2007; Yashayaev and Loder, 2017), includes independently validated and
478 bias-corrected data from multi-section hydrological surveys (i.e., AR7W) in the Labrador
479 Sea, spanning from 1896 to 2020 (this study used 1960-2020 data). These data have not
480 been incorporated into the WOD.

481   The capability of the new product to close the sea level budget and the Earth's energy
482 budget also provides tools for validation. A superior dataset should be capable of closing
483 the sea level and the Earth's energy budgets. The total sea level change has been monitored
484 via satellite altimetry since 1993 (from the University of Colorado
485 https://sealevel.colorado.edu/). The ocean mass change is derived from JPL RL06.1Mv3
486 Mascon Solution GRACE and GRACE-FO data since 2002 (Watkins et al., 2015). For
487 long-term total sea level change since the 1950s, we use a tide-gauge-based reconstruction
488 (Frederikse et al., 2020). During the same period, the estimates of the Greenland ice sheet,
489 Antarctic ice sheet, land water storage, and glacier ice melt contributions from Frederikse
490 et al., (2020) are used to derive ocean mass change. To derive steric sea level, IAP salinity
491 data is used (Cheng et al. 2020). The temperature and salinity data are converted to steric
492 sea level based on the Thermodynamic Equation Of Seawater – 2010 (TEOS-10) standard
493 (McDougall and Barker, 2011).

494   For the energy budget, the ice, land, and atmosphere heat content changes are from
495 (von Schuckmann et al., 2023) from 1960 to the present. Because of the less reliable data
496 before the 1990s for land, sea ice and ice sheets, the other set of land–atmosphere–ice data
497 from 2005–19 is used as in Trenberth, (2022) to investigate the recent changes. The net

498 radiation change at the top of the atmosphere is based on Clouds and Earth's Radiant

499 Energy Systems (CERES) Energy Balanced and Filled (EBAF) data from Loeb et al.,

500 (2021) and Loeb et al., (2018) and Deep-C data from the University of Reading (Liu and

501 Allan, 2022; Liu et al., 2017).

502   Several gridded ocean T/OHC gridded products are used here for inter-comparison,

503 including the IAPv3 (Cheng et al., 2017), the EN4 ocean objective analysis product from

504 the UK Met Office Hadley Centre (Good et al., 2013); the ocean objective analysis product

505 (Ishii et al., 2017) (termed "ISH" hereafter) from JMA, an Argo-only gridded product from

506 SCRIPPS (Roemmich and Gilson, 2009) (termed "RG" hereafter), and an OHC product

507 based on random forest regressions (termed "RFROM" hereafter) using in situ training

508 data from Argo and other sources on a 7-day $\times$ 1/4° $\times$ 1/4° grid with latitude, longitude,

509 time, SSH, and SST as predictors (Lyman and Johnson, 2023). Several datasets available

510 in IPCC-AR6 (Gulev et al., 2023) are used for comparison, including: the PMEL product

511 from Lyman and Johnson, (2014); Machine learning based reconstruction of OHC by

512 Bagnell and DeVries, (2021); BOA product based on refined Barnes successive corrections

513 by the China Argo Real-time Data Center (Li et al., 2017); International Pacific Research

514 Center (IPRC) (2005-2020), von Schuckmann and Le Traon 2011 (KvS11); Green function

515 based OHC estimate derived from SST (Zanna et al., 2019).

516

2.9 Trend calculation and uncertainty estimates

518   The trends in this study have been estimated by a LOWESS approach (Cheng et al.,

519 2022b), i.e., we apply a locally weighted scatterplot smoothing (LOWESS) to the time

520 series (25-year window, equal to an effective 15-years smoothing), and then the OHC

521 difference between the first and the end year is used to calculate the trend. This approach

522 provides an effective method to quantify the local trend by minimizing the impact of year-

523 to-year variability and start/end points.

524   Throughout this paper, the 90 % confidence interval is shown. The uncertainty of

525 trend also follows the approach in Cheng et al., (2022a) based on a Monte Carlo

526 simulation. First, a surrogate OHC series is formed by simulating a new residual series

527 (after removing the LOWESS smoothed time series) based on the AR(1) process and

528 adding it to the LOWESS line. Then a LOWESS trendline is estimated for each surrogate.

529 This process is repeated 1000 times, and 1000 trendlines are available. The 90 %

530 confidence interval for the trendline is calculated based on $\pm$ 1.65 times the standard

531 deviation of all 1000 trendlines of the surrogates. Secondly, the uncertainty in the rate of

532 the OHC is estimated by the 1000 LOWESS trendlines: 1) calculating the rate based on the

533 difference between the first and last annual mean value of the LOWESS trendline in a

534 specific period; 2) calculating ± 1.65 times the standard deviation of the 1000 rate values.

535

536 **3. Results**

537 **3.1 Climatological annual cycle**

538   The annual cycle of the OHC above 2000 m of IAPv4 is compared with IAPv3, ISH,

539 EN4, RG and RFROM (Fig. 6 and Fig. 7) for 2006–2020. There is a consistent annual

540 cycle among different datasets for the global and hemispheric oceans. Globally, the ocean

541 releases heat from boreal spring to autumn and accumulates heat from boreal autumn to

542 spring, which is dominated by the southern hemisphere due to its larger ocean surface area

543 (Fig. 6). The two hemispheres show opposite annual variations in OHC, associated with

544 the annual change of solar radiation and different distribution of land and sea. For the

545 global OHC above 2000 m, IAPv4 shows a positive peak in April and a dip in August,

546 with the magnitude of OHC variation of 60.4 ZJ for IAPv4 (66.9 ZJ for IAPv3), consistent

547 with other datasets: 53.2 ZJ for ISH, 58.1 ZJ for EN4, 69.2 ZJ for RG and 56.6 ZJ for

548 RFROM (where 1 ZJ = 10^{21} J).

549   There are some unphysical variations in the OHC annual variations for IAPv3 (blue

550 lines). For example, the global OHC shows large spikes in January and December, and a

551 big shift from September to October, by contrast, the other three data products show much

552 smoother changes (Fig. 6a). The IAPv3 Arctic OHC (north of 69.5 °N) shows different

553 phase change compared with the other datasets together with a big shift from September to

554 December, and the magnitude of variability is much larger in IAPv3 than other datasets

555 (Fig. 6d). The improvement in IAPv4 is mainly because of the methodology

556 improvements: IAPv3 used 1990–2005 data to construct climatology which suffered from

557 errors related to sparse data coverage, use of "degree distance" instead of "km distance",

558 and other error sources. Therefore, the IAPv4 analysis presents a physically tenable OHC

559 seasonal variation.

560

561
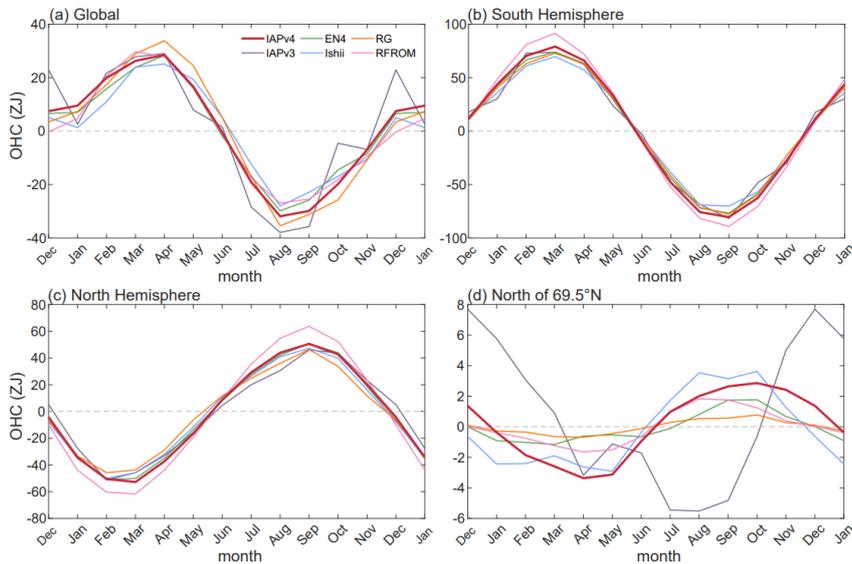
Figure 6: Annual cycle of OHC of upper 2000 m for (a) the global oceans, (b) the
Southern Hemisphere, (c) the Northern Hemisphere and (d) the oceans north of
69.5°N. Five different data products are presented, including IAPv4 (red), IAPv3 (black),
ISH (purple), EN4 (green), RG (orange), and RFROM (pink).

设置了格式：英语（英国）

IAPv4 OHC data shows significant improvements in the Arctic region, reflected in
both the spatial distribution and seasonal variation of OHC. In IAPv3, the maximum upper
2000 m OHC occurs in December, and the minimum OHC occurs in August. However, for
IAPv4, the maximum amounts to 2.9 ZJ in October and decreases to a minimum of −3.4 ZJ
in April. This estimate of the Arctic annual cycle is consistent with a constrained Arctic
OHC estimate with atmospheric data by enforcing energy budget closure (Mayer et al.,
2019). Furthermore, the spread of the OHC annual cycle in the Arctic region across

删除了：T

different datasets is reduced from 5.2 ZJ to 2.5 ZJ, indicating a smaller uncertainty. The
spatial OHC anomaly distribution in the Arctic region of the IAPv4 is more spatially
homogeneous than IAPv3, and IAPv3 appears as rays emerging from the pole which are
not physical (Fig. 7). IAPv4 displays a consistent seasonal variation north of 69.5 °N
mainly because of the changes of the influencing radius from "degrees" to "kilometers".
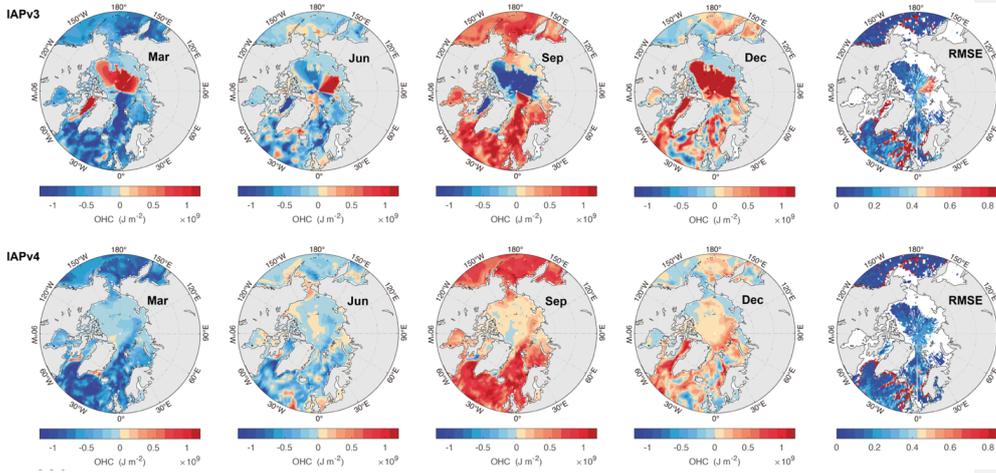
Figure 7: Seasonal distribution of monthly mean upper 2000 m OHC anomalies and root mean square error (RMSE) of OHC 0-2000 m between gridded data and in situ observations. For OHC anomalies, four months are shown: March, June, September, and December. The OHC anomalies are relative to the 2006 – 2020 annual mean. The upper and lower panels are for IAPv3 and IAPv4 products, respectively. The panels in the last column are for annual RMSE for IAPv3 (upper) and IAPv4 (lower), respectively.

3.2 Mixed layer depth

Mixed layer depth (MLD) provides a crucial parameter of upper ocean dynamics relevant for upper-deeper ocean and air-sea interactions. Spatial distributions of the MLD in March and August are shown in Fig. 8 for IAPv4, based on criteria of $\Delta T = 0.2\ ^{\circ}C$ temperature for the 10 m depth temperature. As expected, the seasonal variations of the MLD are generally opposite in the northern and southern hemispheres. The MLD shows a much stronger seasonal variation in the subtropics and midlatitudes (for example, $20°\sim70°$ in both hemispheres) than in other regions (including the tropics, for example, $20°S\sim20°N$), which is manifested as shallower MLD (~20 m) in summer due to strong surface heating that increases stratification, and deeper MLD in winter (>70 m) because of surface cooling and increased surface wind creating stronger mixing.

In the north hemisphere, the maximum MLD occurs during the wintertime in the subpolar North Atlantic deep water formation regions (40 °N ~ 65 °N), with values over

602 500 m in the Iceland Basin. In comparison, in the midlatitudes, the maximum of MLD is

603 generally less than 125 m in the wintertime. The MLD minimum in the north hemisphere is

604 in the summertime, and the values are mostly within 20 m depth. In the Southern

605 Hemisphere, the MLD maximum values (deeper than 300 m) occur between 45 °S and

606 60 °S of the Southern Ocean (north of the Antarctic Circumpolar Current) in the boreal

607 summer where the year-round intense westerly winds are located. The minimum MLD in

608 this region in the boreal winter is less than 70 m. The seasonal variation of the MLD is

609 well established by previous studies (Chu and Fan, 2023; de Boyer Montégut et al., 2004;

610 Holte et al., 2017), and this evaluation confirms that IAPv4 temperature data is capable of

611 reasonably representing the MLD. However, as pointed out by de Boyer Montégut (2004),

612 the MLD estimated from the average temperature profiles might lead to an underestimation

613 of MLD by ~25% compared to the MLD computed from individual profiles based on the

614 same 0.2 °C criterion method. This potential issue needs further investigation.
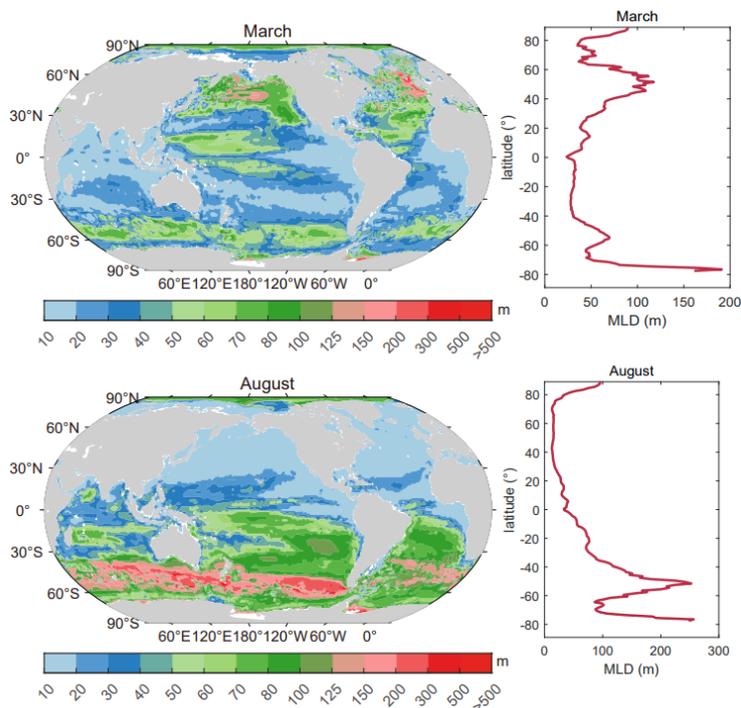
615

616 **Figure 8: Spatial pattern of the climatological mean MLD (left panels) and zonal**

617 **mean MLD (right panels) in March (top) and August (bottom) estimated from the**

618   **IAPv4.** Here, the MLD is calculated using the temperature difference criterion of $\Delta T =$
619   0.2 ℃ between the surface and 10-meter depth.

620

621   **3.3 Sea surface temperature**

622   IAPv4 and IAPv3 temperature time series at 1 m depth (Fig. 9) are compared with
623   four independent SST data products (ERSST5, HadISST, COBE1, and COBE2). All data
624   products including IAPv4 show robust sea surface warming in the global ocean and four
625   main basins since 1955 (Fig. 9). Since the HadISST and COBE2 data did not include the
626   year 2023, we compare the long-term SST trend during 1955–2022 using these products
627   (Fig. 9f). The global-mean IAPv4 SST rate between 1955 and 2022 is 1.01 ± 0.15 ℃
628   century^{-1} (90 % CI), which is within the range of the SST products (ranging from 0.78 to
629   1.05 ℃ century^{-1}). The 1955–2022 trend of IAPv4 SST is slightly weaker than IAPv3 for
630   the global ocean (1.11 ± 0.16 ℃ century^{-1}) and all the ocean basins. The largest difference
631   between IAPv4 and other SST products comes mainly from the Pacific and the Southern
632   Ocean before 1980, associated with sparser in situ observations for both SST and
633   subsurface temperature data.

634   The spatial distribution of long-term SST trends over the 1955–2022 period provides
635   insights into the data consistencies and differences. First, IAPv4 shows a pattern of SST
636   consistent with other datasets (Fig. 10). More rapid warming is found in the poleward
637   western boundary currents regions, such as the East Australian Current and the Gulf
638   Stream. The warmer ocean in the upwelling areas, such as the Tropical Eastern Pacific and
639   Gulf of Guinea, are identified by all data products. The surface warming in the South
640   Indian for IAPv4 data is weaker than for IAPv3, ERSST5, and COBE2 but is more
641   consistent with HadISST and COBE1. The surface cooling to the south of 60 °S can also
642   be found in all the datasets but with some discrepancies in magnitude and locations related
643   to data sparsity. The tropical Pacific SST trends are mostly insignificant in the eastern and
644   south-eastern Pacific Ocean because of the strong inter-annual and decadal fluctuations
645   (Figure not shown).

646
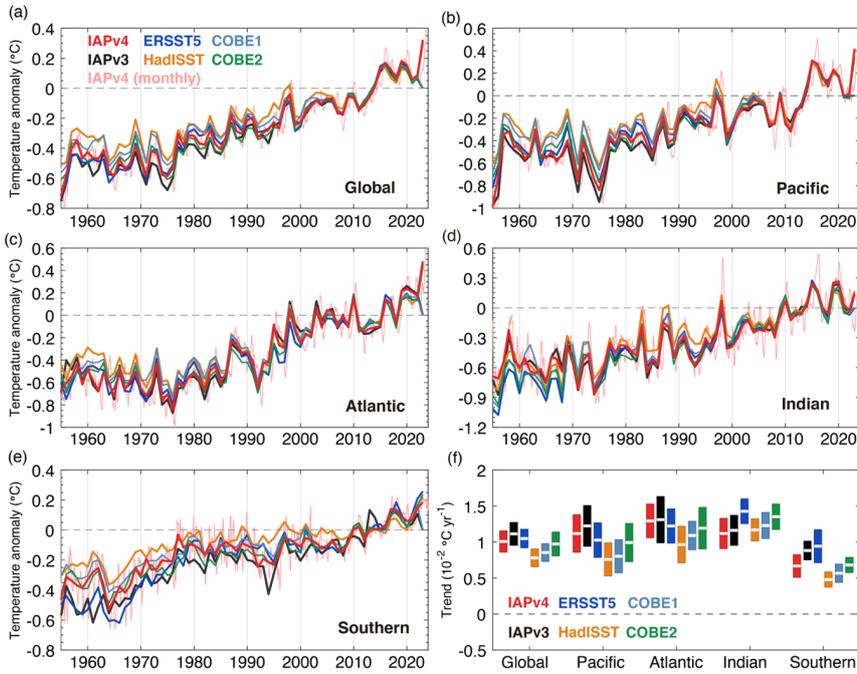
Figure 9: Global and basin time series of SST change for IAPv4, compared with ERSST/HadISST/COBE1/COBE2 and IAPv3 from 1955 to present. (a) Global, (b) Pacific, (c) Atlantic, (d) Indian and (e) Southern oceans (South of 30 °S) (units: °C). (f) shows the warming rate from 1955 to 2022 The pink thin line is the monthly time series of IAPv4 SST and other time series are annual time series of different datasets. The vertical scales are different for different panels. All anomaly time series are relative to a 2006–2020 baseline.

647

648

649

650

651

652

653

654

655
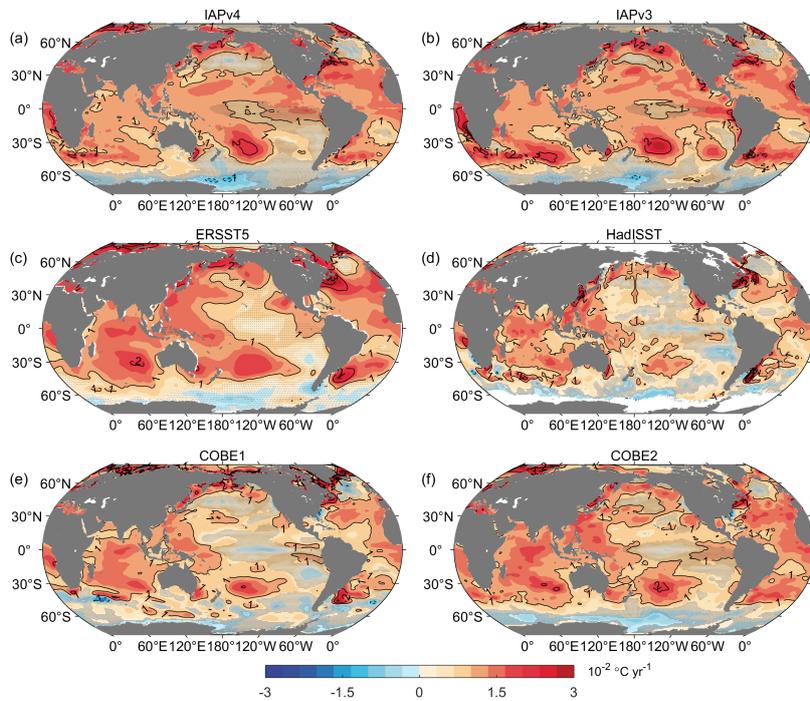
Figure 10: Spatial maps of the SST long-term trends during the 1955–2022 period. (a) IAPv4, (b) IAPv3, (c) ERSST5, (d) HadISST, (e) COBE1 and (f) COBE2 (units: 10^{-2} °C yr^{-1}). The contour line interval is $0.5×10^{-2}$ °C yr^{-1}. The stippling indicates the regions with signals that are not statistically significant (90 % CI).

660

3.4 Global OHC time series

Global OHC time series for 0–700 m, 700–2000 m, 0–2000 m, and 2000-–6000 m layers of IAPv4 (Fig. 11) for 1955–2023 versus IAPv3 show a robust ocean warming, with a linear warming rate of 4.4 ± 0.2 ZJ yr^{-1} (0–700 m), 2.0 ± 0.1 ZJ yr^{-1} (700–2000 m), and 6.4 ± 0.3 ZJ yr^{-1} (0–2000 m). The long-term warming revealed by IAPv4 is greater than IAPv3 (4.1 ± 0.2 ZJ yr^{-1} for 0–700 m, 1.9 ± 0.1 ZJ yr^{-1} for 700–2000 m and 6.0 ± 0.3 ZJ yr^{-1} for 0–2000 m). Before ~1980, bottle bias correction reduces the time-varying systematic warm bias in Nansen bottle data and leads to a stronger warming rate from 1955–1990. The updated MBT and XBT corrections are mainly responsible for the

670 difference between 1980 and 2000 (Cheng et al., 2014; Gouretski and Cheng, 2020). Data

671 QC impacts the intra-seasonal and inter-annual variation of the OHC time series (Tan et

672 al., 2023). Also, because of the application of Bottle/XBT/MBT corrections, IAPv4 shows

673 a stronger upper 2000 m ocean warming trend than most of the other available products

674 assessed in Fig. 12.

675 From 2005–2023, the new IAPv4 product shows stronger warming than IAPv3. The

676 mean upper 2000 m warming rate is 10.7 ± 1.0 ZJ yr^{-1} for IAPv4 and 9.6 ± 1.1 ZJ yr^{-1} for

677 IAPv3 (Fig. 11), mainly because of the replacement of the WOD-QC system by the new

678 CODC-QC system in IAPv4. Tan et al., (2023) indicated that the WOD-QC system had

679 removed more extreme higher temperature values in the regions of warm eddies and

680 marine heat waves than CODC-QC. The IAPv3 700–2000 m OHC shows a much bigger

681 drop in 2018 than IAPv4 (Fig. 11b), while the IAPv4 indicates an approximately linear

682 700–2000 m warming since 2005, resulting in stronger 700–2000 m warming in IAPv4

683 (3.6 ± 0.5 ZJ yr^{-1}) than in IAPv3 (2.9 ± 0.5 ZJ yr^{-1}). Compared with other available

684 products shown in Fig. 12, IAPv4 shows a similar OHC 0–2000 m trend to RFROM from

685 2005–2023, but with stronger warming trends than the two Argo-based products (BOA and

686 SCRIPPS). From 1993–2023, IAPv4 showed a stronger OHC 0–2000 m trend than NCEI,

687 Ishii, OPEN, and Zanna data and a slightly weaker trend than PMEL and RFROM (Fig.

688 12).

689 Since the 1990s, the World Ocean Circulation Experiment (WOCE) provided a global

690 network of abyssal ocean observations, sustained by repeated hydrological lines and a

691 deep-Argo program (Katsumata et al., 2022; Roemmich et al., 2019; Sloyan et al., 2019).

692 These high-quality data provide an opportunity to estimate deep OHC changes below 2000

693 m in this study. IAPv4 provides a new OHC estimate below 2000 m by collecting 5 years

694 of data centered on each month. The result (Fig. 11d) indicates a robust abyssal (2000–

695 6000 m) ocean warming trend since ~1993 of 2.0 ± 0.3 ZJ yr^{-1}. This is higher (within the

696 uncertainty range) than the previous estimate of 1.17 ± 0.5 ZJ yr^{-1} in Purkey and Johnson

697 (2010) but consistent with the recent assessment showing the acceleration of deep ocean

698 warming in the Southwest Pacific Ocean (Johnson et al., 2019).

699

700
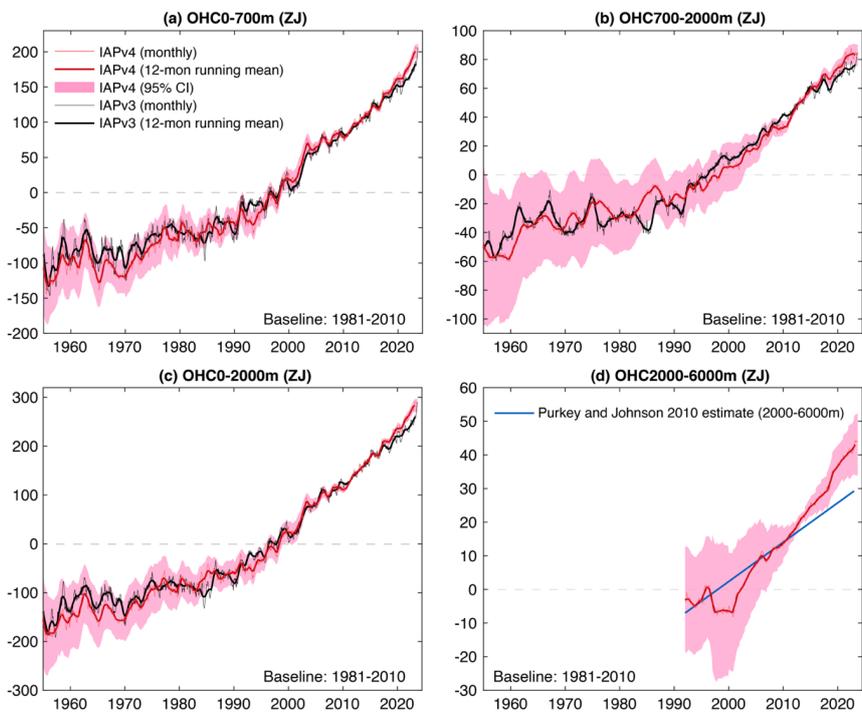
Figure 11: Global OHC time series for 0–700 m (a), 700–2000 m (b), 0–2000 m (c) and 2000–6000 m (d). All-time series are relative to a 1981–2010 baseline. The shading indicates the 90 % confidence interval. The vertical scales are different for different panels. The unit is ZJ.

705
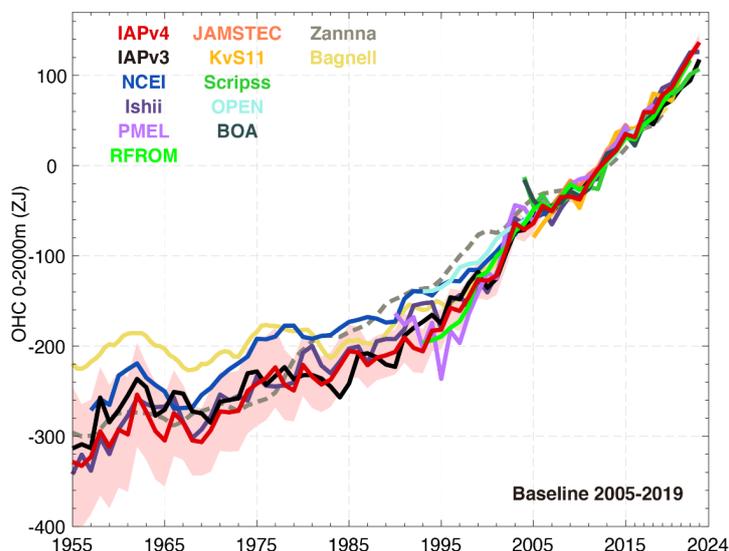
Figure 12: A comparison of annual mean OHC 0-2000 m time series from different data products. Solid and dashed lines represent direct and indirect estimates, respectively, and shading indicates the IAPv4 90% confidence interval (pink shading). OHC anomalies are relative to a 2005–2019 baseline. The plot is updated from Cheng et al. (2022a).

Another feature of IAPv4 is the suppression of month-to-month noise compared to many available data products. Trenberth et al. (2016) noted that the month-to-month variation (quantified by the standard deviation of the monthly dOHC/dt time series) in all *in situ*-based OHC records is much larger than implied by the CERES records, suggesting that the OHC variation on this time scale is most likely spurious. Therefore, the magnitude of the month-to-month variation in the OHC record can be used as a benchmark of the data quality. The standard deviation of the CERES record is 0.67 Wm^{-2} from 2005 to 2023 (Loeb et al., 2018). While IAPv4, IAPv3, ISH, EN4, BOA, NCEI, and SIO data show a standard deviation of dOHC/dt time series of 3.52, 3.52, 7.49, 8.79, 10.05, 11.29, 10.00 Wm^{-2}, respectively for the upper 2000 m (Table 2). Note that differentiation to get the rate of change amplifies noise, and applying a 12-month running smoother significantly knocks down the noise so that the IAPv4 standard deviation becomes 0.75 Wm^{-2}, the smallest among the datasets investigated in this study (Table 2) and is the most physically plausible time series from this noise-level perspective. In addition, Lyman and Johnson's (2013) data

suggest a yearly variance ratio of 1.3 between annual RFROM and CERES data from 2008

to 2021. Using the yearly mean OHCT indicates a ratio of 1.4 at the same period between

IAPv4 and CERES, which is similar to that of RFROM.

Table 2. Characteristics of Month-to-month variation of OHCT compared with CERES. Comparisons of different ocean gridded products: the monthly standard deviation (std dev) of the monthly rates of change of OHC (W m^{-2}); the corresponding standard deviation of the 12-month running mean (13-points are used, with start-point and endpoint weighted by 0.5), and the linear trend with 90% confidence limits (Wm^{-2}) (global surface area). The values are for 2005–2022. The OHC trend for CERES is calculated as the mean of net TOA radiation flux within 2005–2022 multiplied by 0.9, assuming 90% of the EEI stored in the ocean.

Source	Std dev	Std dev (12 month)	OHC Trend (2005–2022)
IAPv4	3.52	0.75	0.66 ± 0.04
IAPv3	3.52	0.79	0.56 ± 0.03
ISH	7.49	1.35	0.63 ± 0.05
EN4	8.79	1.03	0.67 ± 0.04
BOA	10.05	1.16	0.60 ± 0.07
NECI	11.29	1.11	0.61 ± 0.07
SIO	10.00	1.24	0.56 ± 0.08
CERES	0.67	0.33	0.77

3.5 Regional OHC trends

For 1960–2023 (Fig. 13), the IAPv4 trends are slightly weaker than IAPv3 in the

Pacific Ocean but slightly higher in the Atlantic Ocean (Fig. 13), with more than 95 % of

the ocean area showing a warming trend. The polar regions also show remarkable

differences compared to IAPv3 (Section 3.1), mainly because of the change of covariance,

which improves the spatial reconstruction in the polar regions. The IAPv4 shows stronger

warming near the boundary currents regions, mainly because of the improved QC that does

not flag high-temperature anomalies. Nevertheless, the pattern of trends is very similar in

the two versions of data, indicating the robustness of the ocean warming pattern. The

Atlantic Ocean (within 50 °S–50 °N) and the Southern Ocean store more heat than the

other basins, probably associated with the deep convection and subduction processes

750 effectively transporting heat into the deep layers (Cheng et al., 2022a). The cold spots

751 mainly include the Northwest Pacific and subpolar North Atlantic Ocean. In particular, the

752 so-called "warming hole" in the subpolar North Atlantic Ocean can extend to at least 800

753 m and is responsible for decreased OHC in this region. Some studies have linked this

754 fingerprint to the slowdown of AMOC (Rahmstorf et al, 2015; Caesar et al., 2018).
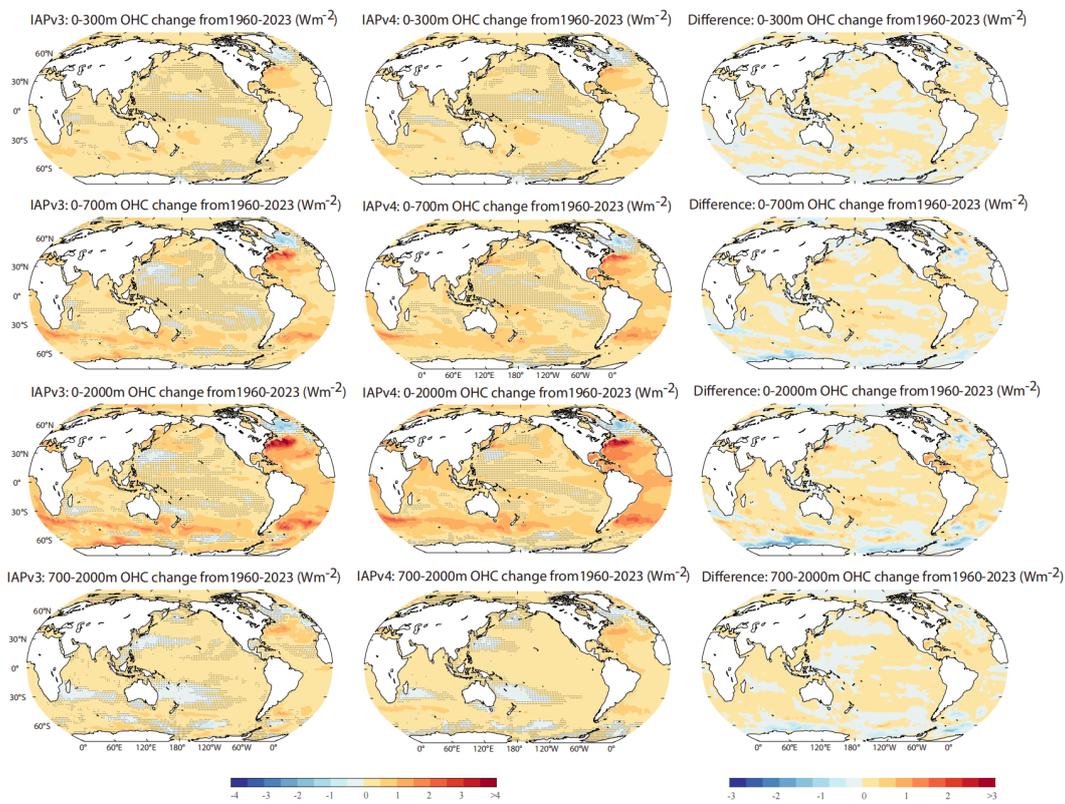
756 **Figure 13: Spatial pattern of the OHC trends for 0–300 m, 0–700 m and 0–2000 m,**

757 **700–2000 m from 1960 to 2023**. The left panels show IAPv3, the middle panels are

758 IAPv4; the right panels are the difference between IAPv4 and IAPv3.

759 For 1991–2023 (Fig. 14), the IAPv4 and IAPv3 pattern is also consistent. A trend

760 pattern mimicking a negative Pacific Decadal Variability (PDV) phase appears in the Pacific

761 for the 0–300 m, 0–700 m, and 0–2000 m OHCs. There is a contrast between the warming

762   trend of the tropical western Pacific and the cooling trend of the tropical eastern Pacific.

763   Some studies have linked this pattern to the natural climate mode (PDV) (England et al.,

764   2014), but some suggest it is a forced change driven by greenhouse gas increases (Fasullo

765   and Nerem, 2018; Mann, 2021). Below 700 m, the 1960–2023 and 1991–2023 trend

766   patterns are similar because deep ocean warming mainly occurs after 1990. Broad warming

767   in most regions, but subtropical oceans in the West Pacific and South Indian oceans show a

768   cooling, which is likely related to the subtropical gyre intensification in the North but a

769   spin-down in the North Pacific Ocean (Zhang et al., 2014).
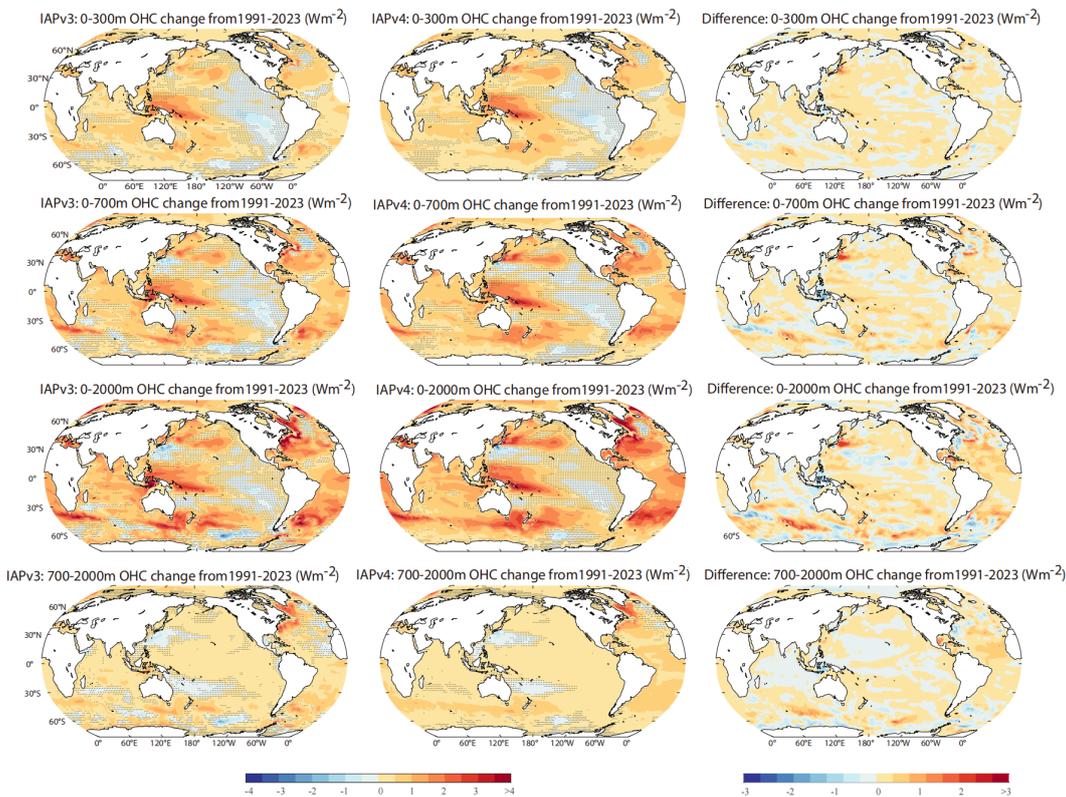
771   **Figure 14: Spatial pattern of the OHC trends for 0–300 m, 0–700 m, 0–2000 m and**

772   **700–2000 m from 1991 to 2023.** The left panels show IAPv3, the middle panels are

773   IAPv4; the right panels are the difference between IAPv4 and IAPv3.

774   Furthermore, the reconstruction of IAPv4 is compared with completely independent

775   observations in the central Labrador Sea (see Data and Methods section for details;

776   Yashayaev, 2007; Yashayaev and Loder, 2017) for the 200-2000 m mean temperature time

777   series (Fig. 15). The direct observations show a substantial decadal variation in the central

778   Labrador Sea, with negative anomalies 1970-2003 and 2015-2020, and positive anomalies

779   1963-1972 and 2004-2014. Reconstructed based on data from WOD, IAPv4 can well

780   represent this decadal variability. The largest difference occurs in 1989, where direct

781   observations show nearly zero anomaly while IAPv4 shows a big negative anomaly; this

782   difference is likely caused by using a time window in IAPv4, which has a smoothing effect

783   on the time series.
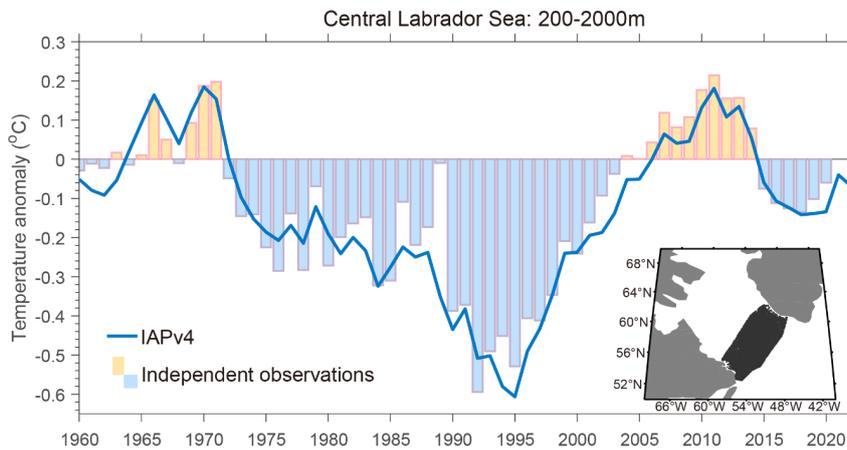
784

785   **Figure 15: Comparison of IAPv4 data with independent observations in the central**

786   **Labrador Sea (304 -310 °E, 55-61 °N) from 1960 to 2020.** The 200-2000 m averaged

787   temperature anomaly time series is shown, and the baseline is 1960-2020. The inner box

788   shows the locations of the independent observations in black dots (showing a total of

789   49,849 profiles).

790

791   **3.6 Ocean meridional heat transport**

792   The ocean meridional heat transport (MHT) is fundamental to maintaining the earth's

793   energy balance. Thus, its change and stability are key to the climate system and its

794   variability. The direct observations of ocean MHT are only possible in several cross-basin

795   sections such as RAPID. The ocean MHT can be derived from the OHC and air-sea heat

flux data (Trenberth and Fasullo, 2017; Trenberth et al., 2019) as follows: we integrate the OHCT, air-sea heat flux and heat gain/loss by sea ice changes from the North Pole southward in the Atlantic Ocean, and solve the energy budget equation, the residual at each latitude is the MHT, i.e.,

$$MHT(\varphi) = \int_{\varphi}^{90} \left[Fs + \frac{dOHC}{dt} + Q_{ice} \right] a \, d\varphi$$

Where a is the Earth's radius, φ is latitude, Fs is net surface heat flux, and Q_{ice} is the heat inferred from the changes of sea ice mass. Consistent with Trenberth et al. (2019), this study uses the sea ice volume data from the Pan-Arctic Ice Ocean Modeling and Assimilation System (PIOMAS; Schweiger et al. 2011), and assumes a constant latent heat of fusion of 3.34×10^5 J kg^{-1} and a density of ice of 900 kg m^{-3}. Both Fs and OHCT are important for the MHT derivation: the integrated air-sea heat flux dominates the magnitude of the MHT, while the OHCT dominates the variability of the MHT (Liu et al., 2020).

The comparison between OHC-derived MHT and RAPID data allows one to check the consistency among various observations. Here, we calculate the Atlantic MHT from April 2004 to December 2022 using IAPv4 OHC and air-sea net heat flux data (F$_S$) derived by TOA net energy flux and atmospheric heat divergence (Fig. 16). F$_S$ is an average of three available products including MAYER2021 (Mayer et al., 2021) TF2018 (Trenberth et al., 2019) and the DEEP-C Version 5.0 from Reading University (Liu and Allan, 2022; Liu et al., 2020). The data are adjusted following Trenberth et al. (2019) approach to ensure zero MHT on the Antarctica coast. The inferred time series of MHT at 26.5 °N from other OHC data sets (IAPv3, Ishii, and EN4) are also shown in Fig. 16, compared with the RAPID observations (Johns et al., 2023).

The Inferred long-term mean (April 2004－December 2022) MHT from the updated IAPv4 OHCT (solid red line with the mean transport of 1.18 PW) is identical to the RAPID observation of 1.18 ± 0.19 PW. Different OHC datasets cause different inter-annual variability in the MHT. It is shown that, from 2008 to 2020, the RAPID MHT agrees best with the IAPv4 estimates with a correlation of 0.52. By comparison, the correlation coefficients between RAPID and IAPv3, EN4, and Ishii are 0.33, 0.51, and 0.49, respectively. Over the entire period of 2005~2022, the IAPv4 lies mostly within the RAPID uncertainty envelope.
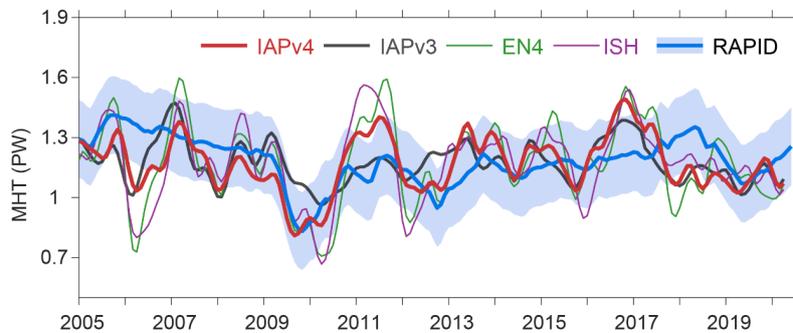
Figure 16: Derived meridional heat transport at 26.5 °N. The 12-month running mean

northward MHT across 26.5 °N of different data sets compared with results from the

RAPID array in PW. The error bars for RAPID in grey are 1.64 σ.

3.7 Inter-annual variability

The year-to-year variation of OHC is strongly influenced by ENSO from global to
regional scales (Cheng et al., 2019; Roemmich and Gilson, 2011). To demonstrate the
change of OHC associated ENSO, Figure 17 shows a Hovmöller diagram of the zonal
upper 2000 m OHC and its change (time derivative of OHC: d(OHC)/dt) in the tropical
Pacific Ocean from 1985 to 2023, compared with the Oceanic Niño Index (ONI). It is
evident that both OHC and OHCT are closely correlated with ENSO.

Before the onset of El Niño events, there is an accumulation of heat (d(OHC)/dt > 0)
in the southern and equatorial tropical Pacific ocean region (20 °S–- 5 °N). The positive
tropical Pacific dOHC/dt leads ONI by ~15 months (with peak correlation >0.5), making it
a precursor of El Niño (Cane and Zebiak 1985; McPhaden, 2012; Lian et al., 2023). In
contrast, heat is redistributed (d(OHC)/dt < 0) from the tropical Pacific (20 °S – 5 °N) to
the North Pacific (5 °N – 25 °N) during and after El Niño (Cheng et al., 2019), with a
maximum correlation >0.8 at 5 months after the El Niño peak. The magnitude of the
prominent change can reach up to 50 Wm^{-2} during the 1997–1998 and 2015–2016 extreme
El Niño events. For the other moderate El Nino events, the regional Pacific OHC change
varies around 10–20 Wm^{-2} (Mayer et al., 2018). This typical heat recharge-discharge
paradigm is crucial in ENSO evolution (Jin, 1997). Correspondingly, the zonal OHC
anomalies in the Pacific Ocean show a warming state (OHC > 0) between ~20 °N and
~5 °S before the peak of El Niño events (with peak correlation >0.7 at 5 months before El

857 Niño peak), followed by a period of cooling (OHC < 0) after the peak of El Niño (with

858 peak correlation >0.7 at 12 months after El Niño peak). These variations are all physically

859 meaningful and indicate that IAPv4 represents regional inter-annual variability, especially

860 associated with ENSO.
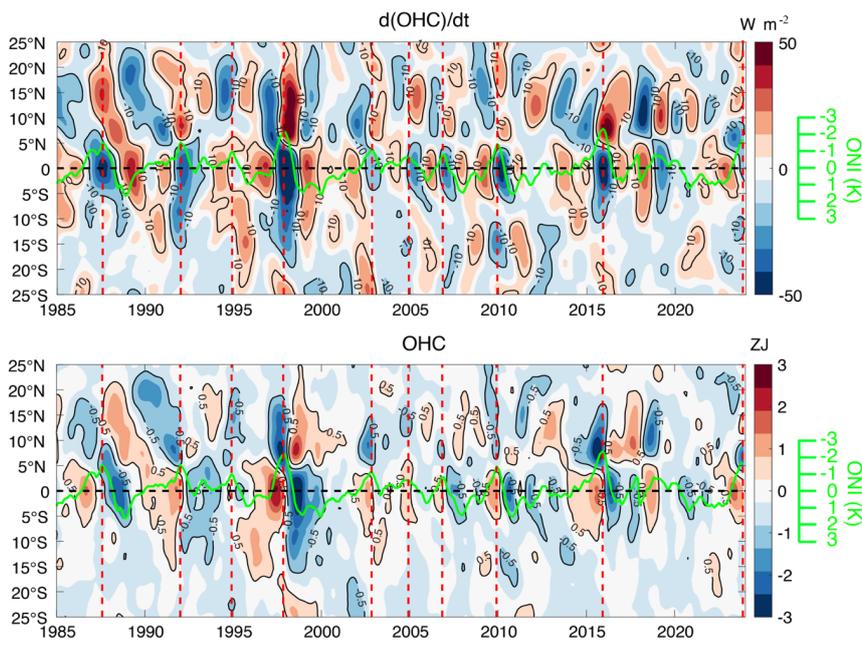
861

862 **Figure 17:** Hovmöller diagrams illustrating the zonal mean (top) upper 2000 m d(OHC)/dt

863 (Wm^{-2}) and (bottom) OHC (ZJ) in each 1 ° latitude band within 25 °S ~ 25 °N in the

864 tropical Pacific basin using IAPv4 data. The ONI is shown in green. Vertical dashed lines

865 denote the peak time of each Niño event.

866

867 **3.8 Ocean and Earth Energy Budget**

868 The EEI provides a critical quantifier of the Earth's energy flow and climate change.

869 It is also policy-relevant because it clearly shows the need to stabilize the climate system.

870 With new T/OHC data, we re-assess the Earth's energy inventory since 1960. The land,

871 atmosphere, and ice contributions are from the estimates obtained by von Schuckmann et

872 al. (2023) for 1960-2023 and by Trenberth (2022) for 2015-2019.

It is evident that the earth has been accumulating heat since 1960. The Earth's heat inventory is 524.0 ± 95.6 ZJ from 1960 to 2023 and 260.3 ± 25.3 ZJ from 2005–2023 based on our data. The upper 700 m ocean, 700–2000 m, 2000 m-bottom, land, ice, and atmosphere contribute to 59.3%, 24.1%, 7.4%, 5.2%, 2.9%, and 1.1% of the total EEI, respectively, since 1960. The relative contribution has changed with time; for instance, since 1993, the contributions are 53.7% (0–700 m ocean), 24.8% (700–2000 m ocean), 12.8% (2000 m–bottom ocean), 4.1% (land), 3.2% (ice), and 1.4% (atmosphere). The land and ice contribution has increased in the recent two decades because of accelerated land and sea ice melting (Comiso et al., 2017; Hugonnet et al., 2021; Minière et al., 2024). From 2005–2019, more reliable land–atmosphere–ice datasets in Trenberth (2022) suggest a non–ocean contribution of 13.4 ZJ. Combined with the results for OHC with IAPv4, the accumulated EEI is 182.5 ZJ with the ocean heat uptake of 169.1 ± 19.7 for 2005–19, consistent with the value of 186.4 ±23.1 ZJ using the non–ocean contribution data by von Schuckmann et al. (2023).

The derived energy inventory has been compared with satellite–based observations at the top of the atmosphere (TOA). Two comparisons are made: (1). integrate the TOA EEI to compare with the energy inventory (Fig. 18); (2) take the time derivative of the annual OHC to compare it with the TOA net radiation flux (Fig. 19). Here we always assume 90% of EEI is stored in the ocean and leads to an increase of OHC (Trenberth et al. 2009; Hansen et al., 2011; von Schuckmann et al., 2020).

The first approach avoids calculating the time derivative of OHC, which exacerbates noise in the time series. The net CERES change has been adjusted to 0.71 Wm^{-2} within 2005–2015, here we adjust the trend of the integrated CERES data to the IAPv4 OHC trend to make it consistent and then compare the variability difference (Fig. 18). The RMSE between DeepC and IAPv4 is 17.9 ZJ and 15.5 ZJ between CERES and IAPv4. The comparison also indicates that the heat inventory shows a stronger heat increase from 2000 to 2005 but too slow heat accumulation during 2005–2010 compared with DeepC and CERES (Fig. 18). This might be due to the data gaps before the Argo network was fully established. DeepC and CERES show stronger heat accumulation since ~2015 than the heat inventory, probably associated with the accelerated abyssal ocean warming found by the Deep-Argo program (Johnson et al., 2019). Furthermore, IAPv4 OHC shows a slightly higher (but consistent within the uncertainty range) Earth's heat uptake compared to von

905 Schuckmann et al. (2023) results by 76.2 ZJ from 1960 to 2020, mainly because the

906 correction of Nansen bottle biases and the updates of XBT and MBT biases in IAPv4 data.

907   The second approach to compare OHC with satellite–based EEI is to calculate the

908 time derivative of OHC. To suppress the month–to–month noises, we estimate annual

909 OHC based on one–year data centered on June (Fig. 19a) and December (Fig. 19b)

910 separately, and then dOHC/dt is calculated with a forward derivative approach based on

911 the annual time series. The annual mean of EEI time series is also used here for

912 comparison (Fig. 19). The IAPv4 and CERES estimates show inter–annual variability with

913 a correlation of 0.44 (the correlation is statistically significant at 90% confidence level,

914 where autocorrelation reduction is taken into account). The higher correlation of IAPv4

915 versus CERES than IAPv3 increases confidence for the new data (correlation of only ~0.15

916 for IAPv3). The trend of dOHC/dt is 0.36 Wm^{-2} dec^{-1} from 2005 to 2023, within the

917 uncertainty range of the CERES record (0.50 ± 0.47 Wm^{-2} dec^{-1} in Loeb et al., 2021).

918 However, it should be noted that the calculation of dOHC/dt is sensitive to the choices of

919 methods, data products, and time periods because of the noises and variability in the OHC

920 time series. A careful analysis of the trend of dOHC/dt (and EEI) is a research priority.

921
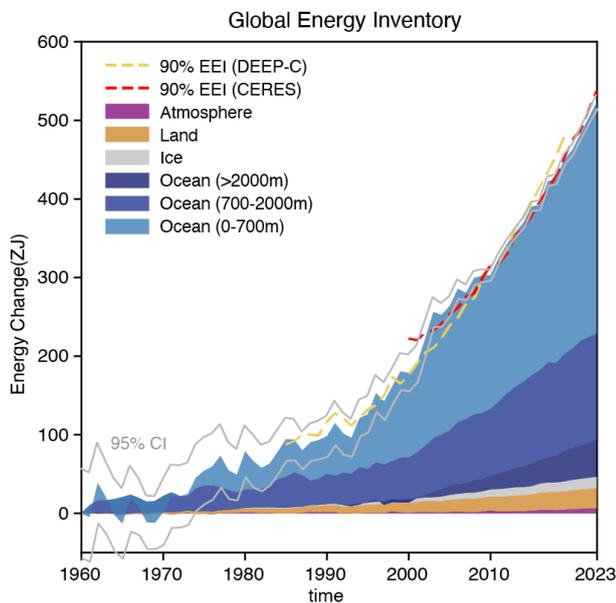
Figure 18: The global energy budget from 1960 to 2023. The atmosphere, land, and ice

923 heat inventory is from von Schuckmann et al., (2023). Integrated EEI from DEEP–C

925 (1985–2018) (Liu and Allan, 2022) and CERES (2001–2023) (Loeb et al., 2021) dataset
926 are presented by dashed lines for comparison, with the trend adjusted to the IAP estimate
927 to account for the arbitrary choice of integration constant. 95% Confidence Interval is
928 presented assuming the independency of different budget components.

929
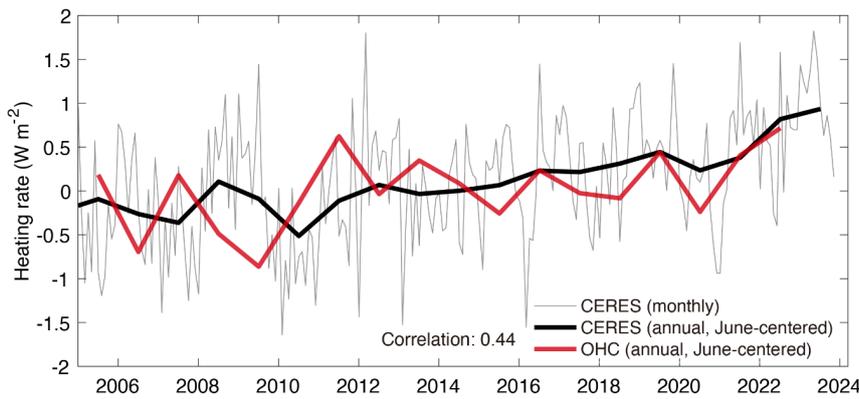
930
931 **Figure 19: Annual ocean heating rate compared with CERES data.** Both annual OHC
932 and CERES EEI data are centred in June. The long–term mean is removed for all-time
933 series.

934

935 **3.9 Steric sea level and sea level budget**

936   The updated IAPv4 data is used to assess the sea level budget for 1960-2023 in
937 combination with other data, including IAP salinity data, glaciers, Greenland, Antarctic ice
938 sheets mass loss from Frederikse et al. (2020) and altimetry sea level record (see Methods
939 section for details). From 1960 to 2023, the observed GMSL rise is 2.07 $\pm$ 0.55 mm yr^{-1}
940 (Frederikse et al., 2020), which is derived by combining tide-gauge observations with
941 estimates of local vertical land motion from permanent Global Positioning System stations
942 and the difference between tide- gauge and satellite altimetry observations (Frederikse et
943 al., 2018). During the same period, the sum of contributors (Glaciers, Greenland and
944 Antarctic ice sheets, land water storage, and steric sea level) yields a mean sea level rise of
945 1.87 $\pm$ 0.42 mm yr^{-1}. Thus, the sea level budget can be closed within a 90% confidence
946 interval. This updated estimate indicates that the steric sea level, Antarctic ice sheet,

删除了：,

删除了：and

删除了：contributions

删除了：.

951 Greenland ice sheet, glaciers, and land water storage contribute to the total sea level with

952 47.3%, 8.6%, 18.0%, 29.1%, and -3.1%, respectively for 1960-2023.

953 To isolate the contribution of the IAPv4 to the sea level budget, we replace the steric

954 sea level estimate in Frederikse et al., (2020) with IAPv4 and re-assess the sea level budget

955 for 1960-2018, 1993-2018 and 2005-2018, and the other components are identical to

956 Frederikse et al. (2020). Two metrics are used to quantify the performance of sea level

957 budget closure: the mean residual error and the temporal root mean square error (RMSD)

958 between the observed GMSL and the sum of contributions. We find that the residual sea

959 level budget based on IAPv4 is 0.20 ± 0.53, 0.11 ± 0.34, 0.47 ± 0.56 mm yr^{-1} for 1960-

960 2018, 1993-2018 and 2005-2018, respectively. These mean residual errors are all smaller

961 than presented in Frederikse et al., (2020), which showed a residual error of 0.29 ± 0.57,

962 0.20 ± 0.34 and 0.54 ± 0.58 mm yr^{-1} for 1960-2018, 1993-2018 and 2005-2018,

963 respectively. The RMSD using IAPv4 (or using steric sea level in Frederikse et al., 2020)

964 is 5.59 (5.35), 4.89 (5.33) and 4.21 (4.51) mm for the above-mentioned three periods,

965 respectively. Therefore, both metrics show that IAPv4 data improves the sea level budget

966 in three typical periods.

967 A similar test is done with the IPCC-AR6 sea level budget estimate (Gulev et al.,

968 2021): the thermosteric sea level estimate in IPCC-AR6 is replaced by IAPv4, and the sea

969 level budget is re-assessed for 1993-2018. IAPv4 suggests a larger thermosteric sea level

970 rise of 1.43 ± 0.16 for 1993-2018 than IPCC (1.31 ± 0.36 mm yr^{-1}) from 1993-2018.

971 Replacing the thermosteric sea level estimate by IAPv4 reduces the mean residual error

972 from 0.40 ± 0.57 to 0.28 ± 0.48 mm yr^{-1}. This suggests that the stronger warming since the

973 1993 revealed by IAPv4 than assessed in IPCC-AR6 (Gulve et al., 2021), seems more

974 realistic.

975 After 2002, the GRACE satellite supported the direct observation of barystatic sea

976 level, which is the sum of the sea level change due to the land water storage, Antarctica ice

977 sheet, Greenland ice sheet, and glaciers. The sea level budget can be obtained by

978 comparing altimetry-based GMSL with the barystatic sea level observed by GRACE and

979 the steric sea level. It is evident that the sea level budget can be closed between 2002 and

980 2015 with ±5 mm residual errors (Fig. 20b). However, after ~2015, the sum of steric and

981 barystatic sea level is smaller than the total sea level rise for all ocean temperature

982 products. Previous studies have attributed this misclosure to salinity data biases (Barnoud

983 et al., 2021), altimetry data errors (Barnoud et al., 2023), and GRACE data errors (Wang et

删除了：again

985 al., 2021). The steric sea level inferred from IAPv4 showed a lower residual (~5 mm)

986 between 2005–2023 than ISH and EN4 data (10~20 mm), indicating that the temperature

987 data might be partly responsible for lack of closure of sea level budget since ~2015. This

988 suggests again that the stronger warming in recent years, as indicated by IAPv4, is more

989 realistic. As discussed in Section 3.4, the QC is mainly responsible for the increased

990 warming of IAPv4 compared with IAPv3 since ~2015 (Fig. 11).

991   Many traditional QC procedures use a static climatological range check to filter out

992 outliers, which does not account for the increase of extreme events with climate change

993 and removes too many extreme (positive) values during the recent period. Thus, we

994 strongly recommend that data product generation groups revisit the QC procedure.

995 Furthermore, as the stronger long-term OHC trends since ~1960 in IAPv4 than in IAPv3

996 are mainly attributed to the bias corrections for Nansen Bottle, MBT, and XBT data, it is

997 also recommended that international groups to revisit the biases in ocean observations.

998

999
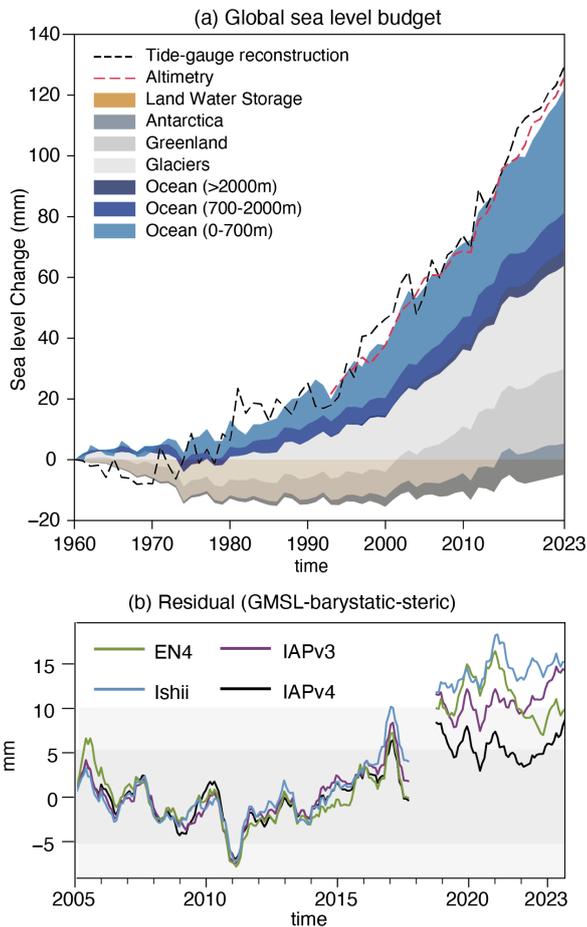
Figure 20: (a) The sea level budget from 1960 to 2023. Observed global mean sea level

1000

for 1960–2023 and the individual contributions from land water storage, Antarctica,

1001

Greenland and Glaciers (Frederikse et al., 2020). The budget is relative to a 1960 baseline.

1002

Here, the land water storage and Glaciers data are through 2018, and a linear extrapolation

1003

is made for 2019–2023. Antarctica ice sheet and Greenland ice sheet changes are estimated

1004

by GRACE after 2018. Tide gauge after 2018 are updated by altimetry. Altimetry sea level

1005

is shown in red dashed line for comparison. (b) Sea level budget residual time series since

1006

2005. The residual of GMSL minus barystatic and steric sea level. The seasonal cycle is

1007

reduced based on 2005–2015 climatology. 6–month running means are shown here to

1008

reduce the noise.

1009

删除了：. A

删除了：smooth

删除了：is applied

1013

4. Data availability

IAPv4 global ocean temperature product is available at

http://dx.doi.org/10.12157/IOCAS.20240117.002 (Cheng et al., 2024a) and

http://www.ocean.iap.ac.cn/.

IAPv4 global ocean heat content product is available at

http://dx.doi.org/10.12157/IOCAS.20240117.001 (Cheng et al., 2024b) and

http://www.ocean.iap.ac.cn/.

The code used in this paper includes data quality control, and the resultant dataset is

available at http://www.ocean.iap.ac.cn/.

The data used in this study (but not generated by this work) are listed below. IAP data are

available at http://www.ocean.iap.ac.cn/. The NCEI/NOAA data are available at

(https://www.ncei.noaa.gov/products/climate-data-records/global-ocean-heat-content). ISH

data from (https://climate.mri-jma.go.jp/pub/ocean/ts/v7.2/). The EN4 data

(https://www.metoffice.gov.uk/hadobs/en4/index.html) For SST: ERSSTv5

(https://www1.ncdc.noaa.gov/pub/data/cmb/ersst/v5/netcdf/); COBE2

(https://psl.noaa.gov/data/gridded/data.cobe2.html); and HadSST3

(https://www.metoffice.gov.uk/hadobs/hadsst3/data/download.html). For sea level data:

AVISO+ GMSL (https://www.aviso.altimetry.fr/en/data/products/ocean-indicators-

products/mean-sea-level.html#c15723), JPL GRACE (https://grace.jpl.nasa.gov/data/get-

data/jpl_global_mascons/), the data in Frederikse et al., (2020) from

(https://zenodo.org/records/3862995). The data in von Schuckmann et al., (2023)

(https://www.wdc-climate.de/ui/entry?acronym=GCOS_EHI_1960-2020). Argo data were

collected and made freely available by the International Argo Program and the national

programs that contribute to it (https://argo.ucsd.edu, https://www.ocean-ops.org). DEEP-C

data from https://doi.org/10.17864/1947.000347; CERES data (https://ceres-

tool.larc.nasa.gov/ord-tool/jsp/EBAFTOA41Selection.jsp); GIOMAS ice volume data

from (https://psc.apl.washington.edu/zhang/Global_seaice/data.html). SCRIPPS data from

(http://sio-argo.ucsd.edu/RG_Climatology.html); BOA data from

(https://argo.ucsd.edu/data/argo-data-products/).

1044

删除了：PIOMAS

删除了：http://psc.apl.uw.edu/research/projects/arctic-sea-ice-volumeanomaly/

5. Summary and Discussion

This paper introduces a new version of the ocean temperature and heat content gridded products and describes the data source and data processing techniques in detail. The key technical advances include the new QC, new or updated XBT/MBT/Bottle/APB bias corrections, new ocean temperature climatology, improved mapping approach, and grid-cell ocean volume corrections. These data and technical advances allow a better estimate of long-term ocean temperature and heat content changes since the mid-1950s from the sea surface down to 2000 m. We show that the new data product could better close the sea level and energy budgets than IAPv3. For rates of change, compared with CERES, the IAPv4 also shows a better correlation from 2005 to 2023 than IAPv3.

Despite several marked improvements, issues needing further investigation remain. Although inter-annual and decadal-scale changes of satellite-based EEI and observational OHC are generally consistent, a mismatch remains between EEI and OHC for their month-to-month variation, as the monthly variation of OHC is still much larger than implied by EEI. There are several possibilities, in our opinion: first, there is substantial heat storage and release for land and ice monthly, which needs to be accurately quantified; second, the accuracy of OHC estimate on a monthly basis still needs to be improved for month-to-month variation because of the limited data coverage; third, the EEI observed by CERES also suffers from sampling biases on a monthly basis (Loeb et al., 2009). Thus, a better understanding of the monthly variation of OHC and EEI is still a research priority. Besides, the failure to close the 2015-2023 sea level budget indicates that the underlying data still has bias problems, which need to be explored and resolved.

Second, the application of CODC-QC in IAPv4 leads to a stronger ocean warming rate in the past decade than WOD-QC used in IAPv3 because WOD-QC removes more positive temperature anomalies than CODC-QC. This could imply that the rate of increase in OHC is still slightly underestimated and deserves an in-depth investigation. Several fundamental questions must be answered: first, are there still real temperature extremes being removed by CODC-QC, such as in small warm/cold eddies? Are the extremes well sampled by the current observation system? If not, what is the impact? Moreover, it is clear that the high latitudes where sea ice occurs are not well sampled and need more attention.

Third, during the development of the data product, we discovered that much metadata relating to the profiles in the World Ocean Database is missing and that much existing metadata is incorrect, also giving rise to duplicate profiles, putting a strain on the overall

quality of a database of oceanic observations. More than ever, long-term concerted efforts are needed to eliminate duplicate profiles and identify and correct missing metadata using statistical methods, expert control, or machine learning techniques. For example, the International Quality-Controlled Database (IQuOD) group is coordinating some activities related to data processing techniques, uncertainty quantification, and improving the overall quality of ocean data (Cowley et al., 2021).

Fourth, the deep ocean changes below 2000 m are estimated based on the currently available data, including data from hydrological sections and Deep-Argo. IAP mapping technique is applied. Because of the lack of independent observations with global ocean coverage, evaluating the deep ocean change estimate is still dicey. Thus, the below-2000 m estimate should be used with caution, as also indicated in previous estimates (Purkey and Johnson, 2010; Desbruyères et al., 2017; Good et al., 2013). A community-agreed evaluation approach for the deep ocean changes is critically needed. Besides, other mapping techniques deserving further investigation include interpolation on isopycnal surfaces (Palmer and Haines, 2009).

Furthermore, the quantification of uncertainty for *in situ* measurements, gridded T/OHC values, and the global OHC estimates need to be improved. IAPv4 only accounts for the instrumental error and sampling/mapping error. In the future, comprehensive quantification of other uncertainty sources will be made, including the choice of climatology, vertical interpolation, XBT/MBT/APB/Bottle corrections, etc. It is also necessary to analyze the correlation between these error sources. This also helps to understand regions with larger uncertainty for OHC estimates, which supports the design of the global ocean observing system.

Author contributions. L.C. has worked on this study's conceptualization, coordination, methodologies, and writing the manuscript. Z.T. worked on *in situ* observation collections, metadata format, and the automated quality control procedure (CODC-QC) development. Y.P. has worked on calculating and comparing the OHC annual cycle, the mixed layer depth, and the MHT among different data sets. V.G. worked on bias correction schemes for MBT, APB, and bottle data and on developing the automated quality control procedure. H.Y. worked on the analysis of inter-annual variability. J.D. has worked on OHC trend calculation and analysis. G.L. worked on SST calculation and its analysis. H. Z. worked on global energy and sea level budget calculations and analyses. Y.L. and Y.J. worked on the

volume correction. All authors have contributed to formal analysis, data validation, and editing of the original draft.

Acknowledgement and Funding. The IAP/CAS analysis is supported by the National Natural Science Foundation of China (Grant no. 42122046, 42076202, 42206208, 42261134536), Strategic Priority Research Program of the Chinese Academy of Sciences (Grant no. XDB42040402), the new Cornerstone Science Foundation through the XPLORER PRIZE, DAMO Academy Young Fellow, Youth Innovation Promotion Association, Chinese Academy of Sciences, National Key Scientific and Technological Infrastructure project "Earth System Science Numerical Simulator Facility" (EarthLab), the Young Talent Support Project of Guangzhou Association for Science and Technology. The calculations in this study were carried out on the ORISE Supercomputer. Some data were collected onboard of R/V Shiyan 6 implementing the Open Research Cruise NORC2022-10+NORC2022-303 supported by NSFC Shiptime Sharing Projects 42149910. NCAR is sponsored by the US National Science Foundation. We acknowledge the World Climate Research Programme's Working Group on Coupled Modelling, which is responsible for CMIP, and we thank the climate modeling groups for producing and making their model output available through the Earth System Grid Federation. The Argo Program is part of the Global Ocean Observing System.

Competing interests. The contact author has declared that none of the authors has any competing interests.

References

Abraham, J. P., Cheng, L., Mann, M. E., Trenberth, K., and von Schuckmann, K.: The ocean response to climate change guides both adaptation and mitigation efforts. Atmospheric and Oceanic Science Letters, 15, 100221, https://doi.org/10.1016/j.aosl.2022.100221, 2022.

Abraham, J. P., and Cheng, L.: Intersection of Climate Change, Energy, and Adaptation. Energies. 15(16), 5886; https://doi.org/10.3390/en15165886, 2022.

Abraham, J. P., Baringer, M., Bindoff, N. L., Boyer, T., Cheng, L. J., Church, J. A., Conroy, J. L., Domingues, C. M., Fasullo, J. T., Gilson, J., Goni, G., Good, S. A.,

Gorman, J. M., Gouret- ski, V., Ishii, M., Johnson, G. C., Kizu, S., Lyman, J. M., Macdonald, A. M., Minkowycz, W. J., Moffitt, S. E., Palmer, M. D., Piola, A. R., Reseghetti, F., Schuckmann, K., Trenberth, K. E., Velicogna, I., and Willis, J. K.: A review of global ocean temperature observations: Implications for ocean heat content estimates and climate change, Rev. Geophys., 51, 450–483, https://doi.org/10.1002/rog.20022, 2013.

Argo: Argo float data and metadata from Global Data Assembly Centre (Argo GDAC). SEANOE, 2000.

Bagnell, A., and DeVries, T.: 20(th) century cooling of the deep ocean contributed to delayed acceleration of Eart''s energy imbalance. Nat. Comm., 12, 4604, https://doi.org/10.1038/s41467-021-24472-3, 2021.

Barker, P. M., and McDougall, T. J.: Two Interpolation Methods Using Multiply-Rotated Piecewise Cubic Hermite Interpolating Polynomials. J. Atmos. Ocean Technol., 37, 605-619, https://doi.org/10.1175/JTECH-D-19-0211.1, 2020.

Barnoud, A., Pfeffer, J., Cazenave, A., Fraudeau, R., Rousseau, V., and Ablain, M.: Revisiting the global mean ocean mass budget over 2005–2020. Ocean Science, 19, 321-334, https://doi.org/10.5194/os-19-321-2023, 2023.

Barnoud, A., Pfeffer, J., Guérou, A., Frery, M.-L., Siméon, M., Cazenave, A., Chen, J., Llovel, W., Thierry, V., Legeais, J.-F., and Ablain, M.: Contributions of Altimetry and Argo to Non-Closure of the Global Mean Sea Level Budget Since 2016. Geophys Res Lett, 48, e2021GL092824, https://doi.org/10.1029/2021GL092824, 2021.

Bindoff, N. L., Cheung, W. W. L., Kairo, J. G., Arístegui, J., Guinder, V. A., Hallberg, R., Hilmi, N., Jiao, N., and Karim, M. S.: Changing Ocean, Marine Ecosystems, and Dependent Communities. In IPCC Special Report on the Ocean and Cryosphere in a Changing Climate [H.-O. Pörtner, D.C. Roberts, V. Masson-Delmotte, P. Zhai, M. Tignor, E. Poloczanska, K. Mintenbeck, A. Alegría, M. Nicolai, A. Okem, J. Petzold, B. Rama, N.M. Weyer (eds.)], Cambridge University Press, Cambridge, UK and New York, NY, USA, pp. 447–587. https://doi.org/10.1017/9781009157964.007, 2019.

Boyer, T., Domingues, C. M., Good, S. A., Johnson, G. C., Lyman, J. M., Ishii, M., Gouretski, V., Willis, J. K., Antonov, J., Wijffels, S., Church, J. A., Cowley, R., and Bindoff, N. L.: Sensitivity of Global Upper Ocean Heat Content Estimates to

Mapping Methods, XBT Bias Corrections, and Baseline Climatologies, J. Climate, 29, 4817–4842, https://doi.org/10.1175/JCLI-D-15- 0801.1, 2016.

Caesar, L., Rahmstorf, S., Robinson, A., Feulner, G., and Saba, V.: Observed fingerprint of a weakening Atlantic Ocean overturning circulation. Nature, 556, 191-196, https://doi.org/10.1038/s41586-018-0006-5, 2018.

Cane, M. A., and Zebiak, S. E.: A theory for El Niño and the southern oscillation. Science, 228, 1085-1087, https://doi.org/10.1126/science.228.4703.1085, 1985.

Cheng, L.: Sensitivity of Ocean Heat Content to Various Instrumental Platforms in Global Ocean Observing System. Ocean-Land-Atmosphere Research, 0, https://doi.org/10.34133/olar.0037, 2024a.

Cheng, L., and Zhu, J.: Uncertainties of the Ocean Heat Content Estimation Induced by Insufficient Vertical Resolution of Historical Ocean Subsurface Observations. J. Atmos. Ocean Technol., 31, 1383-1396, https://doi.org/10.1175/JTECH-D-13-00220.1, 2014.

Cheng, L., and Zhu, J.: Influences of the Choice of Climatology on Ocean Heat Content Estimation. J. Atmos. Ocean Technol., 32, 388-394, https://doi.org/10.1175/JTECH-D-14-00169.1, 2015.

Cheng, L., and Zhu, J.: Benefits of CMIP5 Multimodel Ensemble in Reconstructing Historical Ocean Subsurface Temperature Variations. J. Climate, 29, 5393-5416, https://doi.org/10.1175/JCLI-D-15-0730.1, 2016.

Cheng, L., Zhu, J., Cowley, R., Boyer, T., and Wijffels, S.: Time, Probe Type, and Temperature Variable Bias Corrections to Historical Expendable Bathythermograph Observations. J. Atmos. Ocean. Technol., 31, 1793-1825, https://doi.org/10.1175/jtech-d-13-00197.1, 2014.

Cheng, L., Abraham, J., Goni, G., Boyer, T., Wijffels, S., Cowley, R., Gouretski, V., Reseghetti, F., Kizu, S., Dong, S., Bringas, F., Goes, M., Houpert, L., Sprintall, J., and Zhu, J.: XBT Science: Assessment of Instrumental Biases and Errors, B. Am. Meteorol. Soc., 97, 924–933, https://doi.org/10.1175/BAMS-D-15-00031.1, 2016.

Cheng, L., Trenberth, K. E., Fasullo, J., Boyer, T., Abraham, J., and Zhu, J.: Improved estimates of ocean heat content from 1960 to 2015. Sci. Adv., 3, e1601545, https://doi.org/10.1126/sciadv.1601545, 2017.

Cheng, L., Trenberth, K. E., Fasullo, J. T., Mayer, M., Balmaseda, M., and Zhu, J.: Evolution of Ocean Heat Content Related to ENSO. J. Climate, 32, 3529-3556, https://doi.org/10.1175/jcli-d-18-0607.1, 2019.

1213 Cheng, L., Trenberth, K. E., Gruber, N., Abraham, J. P., Fasullo, J. T., Li, G., Mann, M. E.,
1214   Zhao, X., and Zhu, J.: Improved Estimates of Changes in Upper Ocean Salinity and
1215   the Hydrological Cycle. J. Climate, 33, 10357-10381, https://doi.org/10.1175/JCLI-
1216   D-20-0366.1, 2020.

1217 Cheng, L., von Schuckmann, K., Abraham, J. P., Trenberth, K. E., Mann, M. E., Zanna, L.,
1218   England, M. H., Zika, J. D., Fasullo, J. T., Yu, Y., Pan, Y., Zhu, J., Newsom, E. R.,
1219   Bronselaer, B., and Lin, X.: Past and future ocean warming. Nat. Rev. Earth Env., 3,
1220   776-794, https://doi.org/10.1038/s43017-022-00345-1, 2022a.

1221 Cheng, L., Foster, G., Hausfather, Z., Trenberth, K. E., and Abraham, J.: Improved
1222   quantification of the rate of ocean warming. J. Climate, 35, 4827–4840,
1223   https://doi.org/10.1175/jcli-d-20-0366.1, 2022b.

1224 Cheng, L., Tan, Z., Pan, Y., Zheng, H., Zhu, Y., Wei, W., Du, J., Li, G., Ye, H., Gourteski,
1225   V.: IAP temperature 1° gridded analysis product (IAPv4),
1226   http://dx.doi.org/10.12157/IOCAS.20240117.002, 2024a.

1227 Cheng, L., Tan, Z., Pan, Y., Zheng, H., Zhu, Y., Wei, W., Du, J., Li, G., Ye, H., Gourteski,
1228   V.: IAP global ocean heat content 1° gridded analysis product (IAPv4),
1229   http://dx.doi.org/10.12157/IOCAS.20240117.001, 2024b.

1230 Chu, P. C., and Fan, C.: Global climatological data of ocean thermohaline parameters
1231   derived from WOA18. Scientific Data, 10, 408, https://doi.org/10.1038/s41597-023-
1232   02308-7, 2023.

1233 Comiso, J. C., Meier, W. N., and Gersten, R.: Variability and trends in the Arctic Sea ice
1234   cover: Results from different techniques. J. Geophys. Res.- Oceans, 122, 6883-6900,
1235   https://doi.org/10.1002/2017JC012768, 2017.

1236 Cowley, R., Killick, R. E., Boyer, T., Gouretski, V., Reseghetti, F., Kizu, S., Palmer, M.
1237   D., Cheng, L., Storto, A., Le Menn, M., Simoncelli, S., Macdonald, A. M., &
1238   Domingues, C. M.: International Quality-Controlled Ocean Database (iQuOD) v0.1:
1239   The Temperature Uncertainty Specification. Front. Mar. Sci., 8,
1240   https://doi.org/10.3389/fmars.2021.689695, 2021.

1241 Dangendorf, S., Frederikse, T., Chafik, L., Klinck, J. M., Ezer, T., and Hamlington, B. D.:
1242   Data-driven reconstruction reveals large-scale ocean circulation control on coastal
1243   sea level. Nat. Clim. Change, 11, 514-520, https://doi.org/10.1038/s41558-021-
1244   01046-1, 2021.

1245 de Boyer Montégut, C., Madec, G., Fischer, A. S., Lazar, A., and Iudicone, D.: Mixed
1246   layer depth over the global ocean: An examination of profile data and a profile-based

1247   climatology. J. Geophys. Res.- Oceans, 109, https://doi.org/10.1029/2004JC002378,
1248   2004.

1249 Desbruyères, D., McDonagh, E. L., King, B. A. & Thierry, V. Global and full-depth ocean
1250   temperature trends during the early twenty-first century from Argo and repeat
1251   hydrography. J. Clim. 30, 1985–1997, 2017.

1252 England, M. H., McGregor, S., Spence, P., Meehl, G. A., Timmermann, A., Cai, W.,
1253   Gupta, A. S., McPhaden, M. J., Purich, A., & Santoso, A.: Recent intensification of
1254   wind-driven circulation in the Pacific and the ongoing warming hiatus. Nat. Clim.
1255   Change, 4, 222-227, https://doi.org/10.1038/nclimate2106, 2014.

1256 Fasullo, J. T., and Nerem, R. S.: Altimeter-era emergence of the patterns of forced sea-
1257   level rise in climate models and implications for the future. P. Natl. Acad. Sci., 115,
1258   12944-12949, https://doi.org/10.1073/pnas.1813233115, 2018.

1259 Frederikse, T., Jevrejeva, S., Riva, R. E. M. and Dangendorf, S.: A Consistent Sea-Level
1260   Reconstruction and Its Budget on Basin and Global Scales over 1958–2014. J.
1261   Climate, 31, 1267–1280, https://doi.org/10.1175/JCLI-D-17-0502.1, 2018.

1262 Frederikse, T., Landerer, F., Caron, L., Adhikari, S., Parkes, D., Humphrey, V. W.,
1263   Dangendorf, S., Hogarth, P., Zanna, L., Cheng, L., and Wu, Y.-H.: The causes of sea
1264   level rise since 1900. Nature, 584, 393-397, https://doi.org/10.1038/s41586-020-
1265   2591-3, 2020.

1266 Garcia, H. E., Boyer, T. P., Locarnini, R. A., Baranova, O. K., and Zweng, M. M.: World
1267   Ocean Database 2018: User's Manual., T. E. A.V. Mishonov, NOAA, Silver Spring,
1268   MD., Ed. , 2018

1269 Goni, G. J., Sprintall, J., Bringas, F., Cheng, L., Cirano, M., Dong, S., Domingues, R.,
1270   Goes, M., Lopez, H., Morrow, R., Rivero, U., Rossby, T., Todd, R. E., Trinanes, J.,
1271   Zilberman, N., Baringer, M., Boyer, T., Cowley, R., Domingues, Hutchinson, K.,
1272   Kramp, M., Mata, M. M., Reseghetti, F., Sun, C., Bhaskar Tvs U., Volkov, D.: More
1273   Than 50 Years of Successful Continuous Temperature Section Measurements by the
1274   Global Expendable Bathythermograph Network, Its Integrability, Societal Benefits,
1275   and Future. Fron. Mar. Sci., 6, http://dx.doi.org/10.3389/fmars.2019.00452, 2019.

1276 Good, S. A., Martin, M. J., and Rayner, N. A.: EN4: Quality controlled ocean temperature
1277   and salinity profiles and monthly objective analyses with uncertainty estimates. J.
1278   Geophys. Res. Oceans, 118, 6704-6716, https://doi.org/10.1002/2013jc009067, 2013.

1279 Gouretski, V., and Koltermann, K. P.: How much is the ocean really warming? Geophys.
1280   Res. Lett., 34, L01610, https://doi.org/10.1029/2006GL027834, 2007.

1281 Gouretski, V. and Reseghetti, F.: On depth and temperature biases in bathythermograph
1282   data: Development of a new correction scheme based on analysis of a global ocean
1283   database, Deep Sea Res., 57, 6, 812-833, https://doi.org/10.1016/j.dsr.2010.03.011,
1284   2010.

1285 Gouretski, V., and Cheng, L.: Correction for Systematic Errors in the Global Dataset of
1286   Temperature Profiles from Mechanical Bathythermographs. J. Atmos. Ocean.
1287   Technol., 37, 841-855, https://doi.org/10.1175/jtech-d-19-0205.1, 2020.

1288 Gouretski, V., Cheng, L., and Boyer, T.: On the Consistency of the Bottle and CTD Profile
1289   Data. J. Atmos. Ocean Technol., 39, 1869-1887, https://doi.org/10.1175/JTECH-D-
1290   22-0004.1, 2022.

1291 Gouretski, V., Roquet, F., and Cheng, L.: Measurement biases in ocean temperature
1292   profiles from marine mammal data loggers. J. Atmos. Ocean Technol., submitted,
1293   2024.

1294 Gouretski, V., Kennedy, J., Boyer, T., and Köhl, A.: Consistent near-surface ocean
1295   warming since 1900 in two largely independent observing networks. Geophys. Res.
1296   Lett., 39, https://doi.org/10.1029/2012GL052975, 2012.

1297 Gouretski V, Koltermann K P. 2004. WOCE global hydrographic clima- tology. Berichte
1298   des BSH, 35: 1–52.

1299 Gulev, S. K., Thorne, P. W., Ahn, J., Dentener, F. J., Domingues, C. M., Gerland, S.,
1300   Gong, D., Kaufman, D. S., Nnamchi, H. C., Quaas, J., Rivera, J. A., Sathyendranath,
1301   S., Smith, S. L., Trewin, B., Schuckmann, K. von, and Vose, R. S.: Changing State
1302   of the Climate System Supplementary Material, in: Climate Change 2021: The
1303   Physical Science Basis. Contribution of Working Group I to the Sixth Assessment
1304   Report of the Intergovernmental Panel on Climate Change, edited by: Masson-
1305   Delmotte, V., Zhai, P., Pirani, A., Connors, S. L., Péan, C., Berger, S., Caud, N.,
1306   Chen, Y., Goldfarb, L., Gomis, M. I., Huang, M., Leitzell, K., Lonnoy, E., Matthews,
1307   J. B. R., Maycock, T. K., Waterfield, T., Yelekçi, O., Yu, R., and Zhou, B.,
1308   Cambridge University Press, Cambridge, United Kingdom and New York, NY,
1309   USA, 287– 422, https://doi.org/10.1017/9781009157896.004, 2021.

1310 Hakuba, M. Z., Frederikse, T., and Landerer, F. W.: Earth's Energy Imbalance From the
1311   Ocean Perspective (2005–2019), Geophys. Res. Lett., 48, e2021GL093624,
1312   https://doi.org/10.1029/2021GL093624, 2021.

1313 Hansen, J., Sato, M., Kharecha, P., and von Schuckmann, K.: Eart"'s energy imbalance and
1314   implications. Atmos. Chem. Phys., 11, 13421-13449, https://doi.org/10.5194/acp-11-
1315   13421-2011, 2011.

1316 Hirahara, S., Ishii, M., and Fukuda, Y.: Centennial-Scale Sea Surface Temperature
1317   Analysis and Its Uncertainty. J. Climate, 27, 57-75, https://doi.org/10.1175/JCLI-D-
1318   12-00837.1, 2014.

1319 Holte, J., Talley, L. D., Gilson, J., and Roemmich, D.: An Argo mixed layer climatology
1320   and database. Geophys. Res. Lett., 44, 5618-5626,
1321   https://doi.org/10.1002/2017GL073426, 2017.

1322 Hosoda, S., Ohira, T., and Nakamura, T.: Monthly mean dataset of global oceanic
1323   temperature and salinity derived from Argo float observations. JAMSTEC Report of
1324   Research and Development, 8, https://doi.org/10.5918/jamstecr.8.47, 2008.

1325 Huang, B., Thorne, P. W., Banzon, V. F., Boyer, T., Chepurin, G., Lawrimore, J. H.,
1326   Menne, M. J., Smith, T. M., Vose, R. S., and Zhang, H.-M.: Extended Reconstructed
1327   Sea Surface Temperature, Version 5 (ERSSTv5): Upgrades, Validations, and
1328   Intercomparisons. J. Climate, 30, 8179-8205, https://doi.org/10.1175/JCLI-D-16-
1329   0836.1, 2017.

1330 Hugonnet, R., McNabb, R., Berthier, E., Menounos, B., Nuth, C., Girod, L., Farinotti, D.,
1331   Huss, M., Dussaillant, I., Brun, F., and Kääb, A.: Accelerated global glacier mass
1332   loss in the early twenty-first century. Nature, 592, 726-731,
1333   https://doi.org/10.1038/s41586-021-03436-z, 2021.

1334 IPCC: Annex I: Observational Products [Trewin, B. (ed.)], pp. 2061–2086 pp. , 2021

1335 Ishii, M., and Kimoto, M.: Reevaluation of historical ocean heat content variations with
1336   time-varying XBT and MBT depth bias corrections. J. Oceanogr., 65, 287-299,
1337   https://doi.org/10.1007/s10872-009-0027-7, 2009.

1338 Ishii, M., Shouji, A., Sugimoto, S., and Matsumoto, T.: Objective analyses of sea-surface
1339   temperature and marine meteorological variables for the 2[0]h century using ICOADS
1340   and the Kobe Collection. Int. J. Climatol., 25, 865-879,
1341   https://doi.org/10.1002/joc.1169, 2005.

1342 Ishii, M., Y. Fukuda, S. Hirahara, S. Yasui, T. Suzuki, and K. Sato: Accuracy of Global
1343   Upper Ocean Heat Content Estimation Expected from Present Observational Data
1344   Sets. Sola, 13, 163-167, https://doi.org/10.2151/sola.2017-030, 2017.

1345 Jin, F.-F.: An Equatorial Ocean Recharge Paradigm for ENSO. Part I: Conceptual Model.
1346   J. Atmos. Sci., 54, 811-829, https://doi.org/10.1175/1520-
1347   0469(1997)054%3C0811:AEORPF%3E2.0.CO;2, 1997.

1348 Jin, Y., Li, Y., Cheng, L., Duan, J., Li, R., & Wang, F.. Ocean heat content increase of the
1349   Maritime Continent since the 1990s. Geophysical Research Letters, 51,
1350   e2023GL107526. https://doi.org/10. 1029/2023GL107526, 2024.

1351 Johns, W. E., Elipot, S., Smeed, D. A., Moat, B., King, B, Volkov, D. L., and Smith, R. H.:
1352   Towards two decades of Atlantic Ocean mass and heat transports at 26.5° N.
1353   Philosophical Transactions of the Royal Society A: Mathematical, Physical and
1354   Engineering Sciences, 381, 20220188, 2023.

1355 Johnson, G. C., Purkey, S. G., Zilberman, N. V., and Roemmich, D.: Deep Argo Quantifies
1356   Bottom Water Warming Rates in the Southwest Pacific Basin. Geophys. Res. Lett.,
1357   46, 2662-2669, https://doi.org/10.1098/rsta.2022.0188, 2019.

1358 Katsumata, K., Purkey, S. G., Cowley, R., Sloyan, B. M., Diggs, S. C., Moore, T. S.,
1359   Talley, L. D., and Swift, J. H.: GO-SHIP Easy Ocean: Gridded ship-based
1360   hydrographic section of temperature, salinity, and dissolved oxygen. Scientific Data,
1361   9, 103, https://doi.org/10.1038/s41597-022-01212-w, 2022.

1362 Kennedy, J.: A review of uncertainty in in situ measurements and data sets of sea surface
1363   temperature. Rev. Geophys., 52, 1-32, https://doi.org/10.1002/2013RG000434, 2014.

1364 Levitus, S., Antonov, J. I., Boyer, T. P., Locarnini, R. A., Garcia, H. E., and Mishonov, A.
1365   V.: Global ocean heat content 1955–2008 in light of recently revealed
1366   instrumentation problems. Geophys. Res. Lett., 36,
1367   https://doi.org/10.1029/2008GL037155, 2009

1368 Levitus, S., Antonov, J. I., Boyer, T. P., Baranova, O. K., Garcia, H. E., Locarnini, R. A.,
1369   Mishonov, A. V, Reagan, J. R., Seidov, D., Yarosh, E. S., and Zweng, M. M.: World
1370   ocean heat content and thermosteric sea level change (0–2000 m), 1955–2010,
1371   Geophys. Res. Lett., 39, L10603, https://doi.org/10.1029/2012GL051106, 2012.

1372 Li, G., Cheng, L., Zhu, J., Trenberth, K. E., Mann, M. E., and Abraham, J. P.: Increasing
1373   ocean stratification over the past half-century. Nat. Clim. Change, 10, 1116-1123,
1374   https://doi.org/10.1038/s41558-020-00918-2, 2020.

1375 Li, H., Xu, F., Zhou, W., Wang, D., Wright, J. S., Liu, Z., and Lin, Y.: Development of a
1376   global gridded Argo data set with Barnes successive corrections. J. Geophys. Res.
1377   Oceans, 122, 866-889, https://doi.org/10.1002/2016JC012285, 2017.

1378   Li, Y., Church, J. A., McDougall, T. J., and Barker, P. M.: Sensitivity of Observationally
1379   Based Estimates of Ocean Heat Content and Thermal Expansion to Vertical
1380   Interpolation Schemes. Geophys. Res. Lett., 49, e2022GL101079,
1381   https://doi.org/10.1029/2022GL101079, 2022.
1382   Lian, T., Wang, J., Chen, D., Liu, T. and Wang, D.: A Strong 2023/24 El Niño is Staged by
1383   Tropical Pacific Ocean Heat Content Buildup. Ocean-Land-Atmosphere Research, 2,
1384   0011, https://doi.org/10.34133/olar.0011, 2023.
1385   Liu, C., and Allan, R.: Reconstructions of the radiation fluxes at the top of atmosphere and
1386   net surface energy flux: DEEP-C version 5.0. . a. A. University of Reading Dataset,
1387   Ed., https://doi.org/10.17864/1947.000347, 2022
1388   Liu, C., Allan, R. P., Mayer, M., Hyder, P., Loeb, N. G., Roberts, C. D., Valdivieso, M.,
1389   Edwards, J. M., and Vidale, P.-L.: Evaluation of satellite and reanalysis-based global
1390   net surface energy flux and uncertainty estimates. J. Geophys. Res.- Atmospheres,
1391   122, 6250-6272, https://doi.org/10.1002/2017JD026616, 2017.
1392   Liu, C., Allan, R. P., Mayer, M., Hyder, P., Desbruyères, D., Cheng, L., Xu, J., Xu, F., and
1393   Zhang, Y.: Variability in the global energy budget and transports 1985–2017, Clim.
1394   Dynam., 55, 3381– 3396, https://doi.org/10.1007/s00382-020-05451-8, 2020.
1395   Loeb, N. G., B. A. Wielicki, D. R. Doelling, G. L. Smith, D. F. Keyes, S. Kato, N. Manalo-
1396   Smith, and T. Wong: Toward Optimal Closure of the Earth's Top-of-Atmosphere
1397   Radiation Budget. J. Climate, 22, 748–766, https://doi.org/10.1175/2008JCLI2637.1,
1398   2009.
1399   Loeb, N. G., Johnson, G. C., Thorsen, T. J., Lyman, J. M., Rose, F. G., and Kato, S.:
1400   Satellite and Ocean Data Reveal Marked Increase in Earth's Heating Rate. Geophys.
1401   Res. Lett., 48, https://doi.org/10.1029/2021gl093047, 2021.
1402   Loeb, N. G., Thorsen, T. J., Norris, J. R., Wang, H., and Su, W.: Changes in Earth's energy
1403   budget during and after the "Pause" in global warming: An observational
1404   perspective, Climate, 6, 62, https://doi.org/10.3390/cli6030062, 2018.
1405   Lyman, J. M., and Johnson, G. C.: Estimating Global Ocean Heat Content Changes in the
1406   Upper 1800 m since 1950 and the Influence of Climatology Choice. J. Climate, 27,
1407   1945-1957, https://doi.org/10.1175/JCLI-D-12-00752.1, 2014.
1408   Lyman, J. M., Good, S. A., Gouretski, V. V., Ishii, M., Johnson, G. C., Palmer, M. D.,
1409   Smith, D. M., and Willis, J. K.: Robust warming of the global upper ocean. Nature,
1410   465, 334-337, https://doi.org/10.1038/nature09043, 2010.

Lyman, J. M., and G. C. Johnson, 2023: Global High-Resolution Random Forest
    Regression Maps of Ocean Heat Content Anomalies Using In Situ and Satellite Data.
    J. Atmos. Oceanic Technol., 40, 575–586, https://doi.org/10.1175/JTECH-D-22-
    0058.1.

Mann, M.E., Beyond the Hockey Stick: Climate Lessons from The Common Era, Proc.
    Natl. Acad. Sci., 118 (39) e2112797118, https://doi.org/10.1073/pnas.2112797118,
    2021.

McDougall T. J. and P. M. Barker, 2011: Getting started with TEOS-10 and the Gibbs
    Seawater (GSW) Oceanographic Toolbox, 28pp., SCOR/IAPSO WG127, ISBN 978-
    0-646-55621-5.

Mayer, J., Mayer, M., and Haimberger, L.: Consistency and Homogeneity of Atmospheric
    Energy, Moisture, and Mass Budgets in ERA5. J. Climate, 34, 3955-3974,
    https://doi.org/10.1175/JCLI-D-20-0676.1, 2021.

Mayer, M., Alonso Balmaseda, M., and Haimberger, L.: Unprecedented 2015/2016 Indo-
    Pacific Heat Transfer Speeds Up Tropical Pacific Heat Recharge. Geophys. Res.
    Lett., 45, 3274-3284, https://doi.org/10.1002/2018GL077106, 2018.

Mayer, M., S. Tietsche, L. Haimberger, T. Tsubouchi, J. Mayer, and H. Zuo, 2019: An
    Improved Estimate of the Coupled Arctic Energy Budget. J. Climate, 32, 7915–7934,
    https://doi.org/10.1175/JCLI-D-19-0233.1.

McPhaden, M. J.: A 21st century shift in the relationship between enso sst and warm water
    volume anomalies. Geophys. Res. Lett., 39, 9706,
    https://doi.org/10.1029/2012GL051826, 2012.

McMahon, C. R., Roquet, F., Baudel, S., Belbeoch, M., Bestley, S., Blight, C., Boehme,
    L., Carse, F., Costa, D. P., Fedak, M. A., Guinet, C., Harcourt, R., Heslop, E.,
    Hindell, M. A., Hoenner, X., Holland, K., Holland, M., Jaine, F. R. A., Jeanniard du
    Dot, T., . . . Woodward: Animal Borne Ocean Sensors – AniBOS – An Essential
    Component of the Global Ocean Observing System. Front. Mar. Sci., 8,
    https://doi.org/10.3389/fmars.2021.751840, 2021.

Meyssignac, B., Boyer, T., Zhao, Z., Hakuba, M. Z., Landerer, F. W., Stammer, D., Köhl,
    A., Kato, S., L'Ecuyer, T., Ablain, M., Abraham, J. P., Blazquez, A., Cazenave, A.,
    Church, J. A., Cowley, R., Cheng, L., Domingues, C. M., Giglio, D., Gouretski, V.,
    Ishii, M., Johnson, G. C., Killick, R. E., Legler, D., Llovel, W., Lyman, J., Palmer,
    M. D., Piotrowicz, S., Purkey, S. G., Roemmich, D., Roca, R., Savita, A.,
    Schuckmann, K. von, Speich, S., Stephens, G., Wang, G., Wijffels, S. E., and

Zilberman, N.: Measuring Global Ocean Heat Content to Es- timate the Earth Energy Imbalance, Front. Mar. Sci., 6, 432, https://doi.org/10.3389/fmars.2019.00432, 2019.

Minière, A., von Schuckmann, K., Sallée, J.-B., and Vogt, L.: Robust acceleration of Earth system heating observed over the past six decades. Sci. Rep., 13, 22975, https://doi.org/10.1038/s41598-023-49353-1, 2024

Nerem, R. S., Beckley, B. D., Fasullo, J. T., Hamlington, B. D., Masters, D., and Mitchum, G. T.: Climate-change–driven accelerated sea-level rise detected in the altimeter era. P. Natl. Acad. Sci., 115, 2022-2025, https://doi.org/10.1073/pnas.1717312115, 2018.

O'Carroll, A. G., Armstrong, E. M., Beggs, H. M., Bouali, M., Casey, K. S., Corlett, G. K., Dash, P., Donlon, C. J., Gentemann, C. L., Høyer, J. L., Ignatov, A., Kabobah, K., Kachi, M., Kurihara, Y., Karagali, I., Maturi, E., Merchant, C. J., Marullo, S., Minnett, P. J., Pennybacker, M., Ramakrishnan, B., Ramsankaran, R. Santoleri, R., Sunder, S., Saux Picart, S. Vázquez-Cuervo, J., Wimmer, W.: Observational Needs of Sea Surface Temperature. Front. Mar. Sci., 6, https://doi.org/10.3389/fmars.2019.00420, 2019.

Oliver, E. C. J., Benthuysen, J.A., Darmaraki, S., Donat, M. G., Hobday, A. J., Holbrook, N. J., Schlegel, R.W., and Sen Gupta A., Marine Heatwaves. *Annual review of marine science* **13**, 313-342, https://doi.org/10.1146/annurev-marine-032720-095144, 2021.

Purkey, S. G., and Johnson, G. C.: Warming of Global Abyssal and Deep Southern Ocean Waters between the 1990s and 2000s: Contributions to Global Heat and Sea Level Rise Budgets. J. Climate, 23, 6336-6351, https://doi.org/10.1175/2010jcli3682.1, 2010.

Palmer, M. D., and K. Haines: Estimating Oceanic Heat Content Change Using Isotherms. J. Climate, 22, 4953–4969, https://doi.org/10.1175/2009JCLI2823.1, 2009.

Rahmstorf, S., Box, J., Feulner, G., Mann, M.E., Robinson, A., Rutherford, S., Schaffernicht, E. Exceptional 20th-Century slowdown in Atlantic Ocean overturning, *Nature Climate Change*, 5, 475–480, 2015.

Rayner, N. A., Parker, D. E., Horton, E. B., Folland, C. K., Alexander, L. V., Rowell, D. P., Kent, E. C., and Kaplan, A.: Global analyses of sea surface temperature, sea ice, and night marine air temperature since the late nineteenth century. J. Geophys. Res.-Atmospheres, 108, https://doi.org/https://doi.org/10.1029/2002JD002670, 2003.

Reiniger, R. F., and Ross, C. K.: A method of interpolation with application to oceanographic data. Deep Sea Research, 15, 185-193, https://doi.org/10.1016/0011-7471(68)90040-5, 1968.

Rhein, M., S.R. Rintoul, S. Aoki, E. Campos, D. Chambers, R.A. Feely, S. Gulev, G.C. Johnson, S.A. Josey, A. Kostianoy, C. Mauritzen, D. Roemmich, L.D. Talley and F. Wang, 2013: Observations: Ocean. In: Climate Change 2013: The Physical Science Basis. Contribution of Working Group I to the Fifth Assessment Report of the Intergovernmental Panel on Climate Change [Stocker, T.F., D. Qin, G.-K. Plattner, M. Tignor, S.K. Allen, J. Boschung, A. Nauels, Y. Xia, V. Bex and P.M. Midgley (eds.)]. Cambridge University Press, Cambridge, United Kingdom and New York, NY, USA.

Roemmich, D., and Gilson, J.: The 2004–2008 mean and annual cycle of temperature, salinity, and steric height in the global ocean from the Argo Program. Prog. Oceanogr., 82, 81-100, https://doi.org/10.1016/j.pocean.2009.03.004, 2009.

Roemmich, D., and Gilson, J.: The global ocean imprint of ENSO. Geophys. Res. Lett., 38, https://doi.org/10.1029/2011GL047992, 2011.

Roemmich, D., Alford, M. H., Claustre, H., Johnson, K., King, B., Moum, J., Oke, P., Owens, W. B., Pouliquen, S., Purkey, S., Scanderbeg, M., Suga, T., Wijffels, S., Zilberman, N., Bakker, D., Baringer, M., Belbeoch, M., Bittig, H. C., Boss, E., . . . Yasuda, I.: On the Future of Argo: A Global, Full-Depth, Multi-Disciplinary Array. Front. Mar. Sci., 6, 2019.

Savita, A., and Coauthors: Quantifying Spread in Spatiotemporal Changes of Upper-Ocean Heat Content Estimates: An Internationally Coordinated Comparison. J. Climate, 35, 851–875, https://doi.org/10.1175/JCLI-D-20-0603.1, 2022.

Schweiger, A., R. Lindsay, J. Zhang, M. Steele, H. Stern, and R. Kwok: Uncertainty in modeled Arctic sea ice volume. J. Geophys. Res., 116, C00D06, https://doi.org/10.1029/ 2011JC007084, 2011.

Sloyan, B. M., Wanninkhof, R., Kramp, M., Johnson, G. C., Talley, L. D., Tanhua, T., McDonagh, E., Cusack, C., O'Rourke, E., McGovern, E., Katsumata, K., Diggs, S., Hummon, J., Ishii, M., Azetsu-Scott, K., Boss, E., Ansorge, I., Perez, F. F., Mercier, H., . . . Campos, E.: The Global Ocean Ship-Based Hydrographic Investigations Program (GO-SHIP): A Platform for Integrated Multidisciplinary Ocean Science. Front. Mar. Sci., 6, 2019.

1510 Sun, D., Li, F., Jing, Z. et al. Frequent marine heatwaves hidden below the surface of the
1511   global ocean. Nat. Geosci. 16, 1099–1104, https://doi.org/10.1038/s41561-023-
1512   01325-w, 2023.
1513 Su, H. et al. OPEN: a new estimation of global ocean heat content for upper 2000 meters
1514   from remote sensing data. *Remote Sens*, https://doi.org/10.3390/rs12142294, 2020.
1515 Tan, Z., Zhang, B., Wu, X., Dong, M., and Cheng, L.: Quality control for ocean
1516   observations: From present to future. Science China Earth Sciences, 65, 215-233,
1517   https://doi.org/10.1007/s11430-021-9846-7, 2022.
1518 Tan, Z., Cheng, L., Gouretski, V., Zhang, B., Wang, Y., Li, F., Liu, Z., & Zhu, J.: A new
1519   automatic quality control system for ocean profile observations and impact on ocean
1520   warming estimate. Deep Sea Research Part I: Oceanographic Research Papers, 194,
1521   103961, https://doi.org/10.1016/j.dsr.2022.103961, 2023.
1522 Trenberth, K. E.: The Changing Flow of Energy Through the Climate System.
1523   Cambridge University Press., https://doi.org/10.1017/9781108979030, 2022.
1524 Trenberth, K. E., and Fasullo, J. T.: Atlantic meridional heat transports computed from
1525   balancing Earth's energy locally. Geophys. Res. Lett., 44, 1919-1927,
1526   https://doi.org/10.1002/2016gl072475, 2017.
1527 Trenberth, K. E., Fasullo, J. T., and Kiehl, J.: Earth's Global Energy Budget Bull. Am.
1528   Meteorol. Soc., 90, 311-324, https://doi.org/10.1175/2008bams2634.1, 2009.
1529 Trenberth, K. E., Fasullo, J. T., Von Schuckmann, K., and Cheng, L.: Insights into Earth's
1530   Energy Imbalance from Multiple Sources. J. Climate, 29, 7495-7505,
1531   https://doi.org/10.1175/jcli-d-16-0339.1, 2016.
1532 Trenberth, K. E., Zhang, Y., Fasullo, J. T., and Cheng, L.: Observation-Based Estimates of
1533   Global and Basin Ocean Meridional Heat Transport Time Series. J. Climate, 32,
1534   4567-4583, https://doi.org/10.1175/jcli-d-18-0872.1, 2019.
1535 von Schuckmann, K., and Le Traon, P. Y.: How well can we derive Global Ocean
1536   Indicators from Argo data? Ocean Sci., 7, 783-791, https://doi.org/10.5194/os-7-783-
1537   2011, 2011.
1538 von Schuckmann, K., Cheng, L., Palmer, M. D., Hansen, J., Tassone, C., Aich, V.,
1539   Adusumilli, S., Beltrami, H., Boyer, T., Cuesta-Valero, F. J., Desbruyères, D.,
1540   Domingues, C., García-García, A., Gentine, P., Gilson, J., Gorfer, M., Haim- berger,
1541   L., Ishii, M., Johnson, G. C., Killick, R., King, B. A., Kirchengast, G.,
1542   Kolodziejczyk, N., Lyman, J., Marzeion, B., Mayer, M., Monier, M., Monselesan, D.
1543   P., Purkey, S., Roemmich, D., Schweiger, A., Seneviratne, S. I., Shepherd, A., Slater,

D. A., Steiner, A. K., Straneo, F., Timmermans, M.-L., and Wijffels, S. E.: Heat stored in the Earth system: where does the energy go?, Earth Syst. Sci. Data, 12, 2013–2041, https://doi.org/10.5194/essd-12-2013-2020, 2020.

von Schuckmann, K., Palmer, M. D., Trenberth, K. E., Cazenave, A., Chambers, D., Champollion, N., Hansen, J., Josey, S. A., Loeb, N., Mathieu, P.-P., Meyssignac, B., and Wild, M.: An imperative to monitor Earth's energy imbalance, Nat. Clim. Change, 6, 138–144, https://doi.org/10.1038/nclimate2876, 2016.

von Schuckmann, K. Minière, A. Gues, F. Cuesta-Valero, F. J. Kirchengast, G. Adusumilli, S. Straneo, F. Ablain, M. Allan, R. P. Barker, P. M. Beltrami, H. Blazquez, A. Boyer, T. Cheng, L. Church, J. Desbruyeres, D. Dolman, H. Domingues, C. M. García-García, A. Giglio, D. Gilson, J. E. Gorfer, M. Haimberger, L. Hakuba, M. Z. Hendricks, S. Hosoda, S. Johnson, G. C. Killick, R. King, B. Kolodziejczyk, N. Korosov, A. Krinner, G. Kuusela, M. Landerer, F. W. Langer, M. Lavergne, T. Lawrence, I. Li, Y. Lyman, J. Marti, F. Marzeion, B. Mayer, M. MacDougall, A. H. McDougall, T. Monselesan, D. P. Nitzbon, J. Otosaka, I. Peng, J. Purkey, S. Roemmich, D. Sato, K. Sato, K. Savita, A. Schweiger, A. Shepherd, A. Seneviratne, S. I. Simons, L. Slater, D. A. Slater, T. Steiner, A. K. Suga, T. Szekely, T. Thiery, W. Timmermans, M. L. Vanderkelen, I. Wjiffels, S. E. Wu, T. Zemp, M.: Heat stored in the Earth system 1960–2020: where does the energy go? Earth Syst. Sci. Data, 15, 1675-1709, https://doi.org/10.5194/essd-15-1675-2023, 2023.

Wang, F., Shen, Y., Chen, Q., and Sun, Y.: Reduced misclosure of global sea-level budget with updated Tongji-Grace2018 solution. Sci Rep-Uk, 11, 17667, https://doi.org/10.1038/s41598-021-96880-w, 2021.

Watkins, M. M., Wiese, D. N., Yuan, D. N., Boening, C., and Landerer, F. W.: Improved methods for observing Earth's time variable mass distribution with GRACE using spherical cap mascons. J. Geophys. Res.- Solid Earth, 120, 2648-2671, https://doi.org/10.1002/2014JB011547, 2015.

Wijffels, S. E., Willis, J., Domingues, C. M., Barker, P., White, N. J., Gronell, A., Ridgway, K., and Church, J. A.: Changing Expendable Bathythermograph Fall Rates and Their Impact on Estimates of Thermosteric Sea Level Rise. J. Climate, 21, 5657-5672, https://doi.org/10.1175/2008jcli2290.1, 2008.

WMO: State of the Global Climate 2021, WMO-No. 1290, 2022.

1576 Wong, A. P. S., Wijffels, S. E., Riser, S. C., et al.: Argo Data 1999–2019: Two Million
1577   Temperature-Salinity Profiles and Subsurface Velocity Observations From a Global
1578   Array of Profiling Floats, https://doi.org/10.3389/fmars.2020.00700, 2020.
1579 Zanna, L., Khatiwala, S., Gregory, J. M., Ison, J. & Heimbach, P. Global reconstruction of
1580   historical ocean heat storage and transport. *Proc. Natl Acad. Sci. USA* 116, 1126–
1581   1131, https://doi.org/10.1073/pnas.1808838115, 2019.
1582 Zhang, B. et al. CAS-Ocean Data Center, Global Ocean Science Database (CODCv1):
1583   temperature. Marine Science Data Center of the Chinese Academy of Science,
1584   doi:10.12157/IOCAS.20230525.001 (2024).
1585 Zhang, X., Church, J. A., Platten, S. M., and Monselesan, D.: Projection of subtropical
1586   gyre circulation and associated sea level changes in the Pacific based on CMIP3
1587   climate models. Clim. Dyn., 43, 131-144, https://doi.org/10.1007/s00382-013-1902-
1588   x, 2014.
1589